Design and synthesis of metal-based chemotherapeutic agents for targeted DNA interactions or DNA repair pathway modulation

Griend, C.J. van de

Chapter 4

Photocaging of RAD51 inhibitor by ruthenium

Corjan van de Griend, Maarten van Ginkel, Anita Milisav, Ludo R. Bretin, Amanda Harris, Yurii Husiev, Maxime A. Siegler, Sylvia E. Le Dévédec, Remus T. Dame, Sylvestre Bonnet.

Abstract

The photocaging of biologically active compounds is a well-established method to increase the tissue selectivity of the treatment, as photocaged compounds remain inert in the dark but recover their activity by local activation using visible light. DNA repair inhibitors used in chemotherapy are especially interesting compounds to photocage: on the one hand, a wide variety of cancers show mutations in the DNA repair pathways, but on the other hand one does not want to impede DNA repair in the whole body. Here, we report the synthesis and characterization of compound [**1**]Cl_2, a ruthenium-based photocaged version of B0Cl. B0Cl is an improved analog of B02, a well-known RAD51 inhibitor that blocks double strand break repair via homologous recombination. The quantum yield for light-induced uncaging of B0Cl from [**1**]Cl_2 was determined to be 0.063 in MeCN upon green light irradiation (505 nm) while the inhibitor remained bound to ruthenium in the dark. The light-activated cytotoxicity (EC_{50}) of [**1**]Cl_2 in two uveal melanoma cell lines, OMM2.5 and MM66, was 2.7 µM and 3.3 µM, respectively. Immunofluorescence staining showed an increase of γH2AX foci upon light activation of [**1**]Cl_2 but this increase was minimal in comparison with the double-strand breaks induced by doxorubicin. Combination treatment of [**1**]Cl_2 and doxorubicin resulted in an increase of γH2AX foci in the dark while RAD51 foci decreased upon light activation, which is consistent with the successful photorelease of the B0Cl inhibitor. These initial results demonstrate that the B0Cl inhibitor is successfully caged in [**1**]Cl_2 and could be photoreleased in cells to reduce homologous recombination activity.

4.1 Introduction

The photocaging of protein inhibitors is a reliable method to increase the selectivity of traditional chemotherapeutic inhibitors towards cancerous tissues.[1–4] Although purely organic photocaging strategies have been described, ruthenium-based photocaging is also a very powerful approach that utilizes the dark stability of coordination bonds involving ruthenium(II) polypyridyl compounds, combined with their specific photosubstitution properties.[5–9] In the dark, the "caged" inhibitor remains bound to the ruthenium complex, which usually makes it biologically inert. However, the prodrug can be re-activated upon local light irradiation of the diseased tissues, which releases the free inhibitor from the metal center. The biological activity of the light-activated ruthenium-inhibitor conjugate may result either from the sole action of the inhibitor, or from the combined action of the inhibitor and of the metal-based photoproduct. The latter may be facilitated by available coordination sites on the metal complex, or by other types of photoreactivities, such as the ability to generate singlet oxygen. Zamora *et al.* reported two cytochrome P450 inhibitors caged by the $[Ru(bpy)_2(N)_2]^{2+}$ scaffold.[10] Upon light activation the two coordinated inhibitors were successfully released, while the ruthenium center induced further DNA damage. The interactions of metal complexes and DNA are well documented ever since the discovery of the

DNA cross-linking mechanism of cisplatin.[11–13] However, cisplatin and its more recently developed derivatives carboplatin and oxaliplatin, are still plagued by severe side effects and resistances, which limit their therapeutic efficacy.[14,15]

Although the mechanism of tumor-acquired resistance to chemotherapy is complex, one of its drivers is the enhanced repair of platinum-induced DNA damage.[16] Intrinsically, cells have elaborate pathways to repair DNA damage, which represents a set of chemically distinct modifications of the DNA that induces mistakes in the transcription to RNA and proteins. For example, bases themselves might be damaged, there might be replication mistakes, or one or two of the DNA strands may be interrupted by the cleaving action of reactive oxygen species (ROS) that appear naturally or as a result of ionizing radiation.[17] Overall, all types of DNA damage can be repaired by dedicated enzymatic processes, and some of these repair pathways likewise allow for the repair of chemotherapy-induced DNA damage. When over-expressed in cancer cells, DNA repair pathways may hence limit the effectiveness of anticancer treatments that target DNA.[18]

A promising alternative to conventional platinum-based chemotherapy is the combination of a DNA damage inducer with an inhibitor of the corresponding DNA repair pathway. Schürmann *et al.* screened various DNA repair pathway inhibitors in combination with the anticancer drug doxorubicin (Dox), which works by inducing double-strand break (DSB). They found the highest synergy in HCT-116 colon carcinoma cells using B02, a known RAD51 inhibitor.[19] Alagpulinsa *et al.* also reported a synergistic effect between Dox and RAD51 inhibitor B02, this time in multiple myeloma.[20] RAD51 is a key protein for the repair of DSB in a pathway called homologous recombination (HR). Elevated expression levels of RAD51 is correlated with poor prognoses for cancer patients, due to the observed resistance to DNA damage induced by chemotherapeutic drugs.[20] Recently Ward *et al.* reported structure-activity relationships for a library of compounds based upon the previously established RAD51 inhibitor B02.[21] The addition of a para-chloro substituent on the phenyl group resulted in B0Cl, an improved RAD51 inhibitor with up to 15-fold enhanced inhibition of cell growth in comparison to B02, and a substantial decrease of IC_{50} values, in a range of triple-negative breast cancer cell lines.

Here, we explored the photocaging of RAD51 inhibitors by ruthenium(II) polypyridyl compounds, and looked for synergies between the biological activity of the ruthenium photocaging group, which may induce DSB formation in DNA upon light irradiation, and the inhibitor of DNA repair released by light activation. This study started with the coordination of RAD51 inhibitor B02, its improved derivative B0Cl, or its less active analogue B0Ref (Figure 1), to a set of ruthenium-based photocaging groups $[Ru(tpy)(NN)(L)]^{2+}$ where tpy=2,2':6',2''-terpyridine, NN is either biq (biq=2,2'-biquinoline), dppz (dppz=dipyrido[3,2-a:2',3'-c]phenazine), or dppn (dppn= (benzo[i]dipyrido[3,2-a,2',3'-c]phenazine), and L is the pyridine-based RAD51 inhibitor B0Ref, B02, or B0Cl.

The different ruthenium-based caging groups differ by their bidentate ligand NN: while biq induces steric hindrance in the ruthenium complex that improves photosubstitution quantum yields, dppz is a renowned DNA intercalator, and dppn makes, upon coordination to ruthenium, complexes that are excellent at generating $^1O_2$.

The therapeutic effect of the compounds was studied in uveal melanoma (UM) cell lines OMM2.5 and MM66. UM is a severe form of cancer where almost 50% of patients develop metastatic disease, often in the liver, and is usually fatal within 1 year.[22] Patients developing the metastatic disease have dismal prognosis due to a lack of effective therapies. Although recently the FDA approved the nitrogen mustard alkylating agent Melphalan for the treatment of metastatic uveal melanoma, the development of an effective and selective treatment remains crucial due to side effects of this drug.[23]

In this study, our primary objective is to evaluate the effectiveness of ruthenium photocaged B02 analogues in phototherapy for the treatment of uveal melanoma (UM). To achieve this goal, we synthesized 5 novel ruthenium complexes bound to B02 analogues and fully characterized their photophysical and photochemical properties, ultimately identifying the optimal prodrug candidate. Subsequently, we evaluated the prodrug's biological efficacy and its relevance in a biological context, including the assessment of the cytotoxicity in both the dark and after light irradiation as well as their cellular uptake under normoxic (O_2 = 21%) and hypoxic (O_2 =1%) conditions. This was followed by the immunofluorescence imaging of γH2Ax foci in OMM2.5 cells to study DSB formation upon photoactivation of the complexes. Finally, the combined application of doxorubicin and [**1**]Cl_2 was studied by immunofluorescence imaging of γH2Ax and RAD51 foci in MM66 cells.

4.2 Synthesis

An overview of the RAD51 inhibitors, bidentate ligands, and formulae of the prepared ruthenium compounds [**1**]Cl_2-[**6**]Cl_2 are shown in Figure 1. The dppz and dppn ligand were synthesized according to literature procedure.[24] The three inhibitors B0Cl, B02 and B0Ref were synthesized by combining two reactions described in the literature; the resulting two-step synthesis is convenient and robust, and afforded all three inhibitors in good yields (42-61%). The first step is a condensation reaction of 2-methyl-4H-3,1-benzoxazin-4-one with one of the three benzyl amides necessary for making B0Cl, B02 or B0Ref.[25] This procedure replaced the microwave reaction described in the literature and allowed for larger scale reaction (5 g). The products were isolated by extraction and used without further purification in the subsequent Knoevenagel condensation adapted from Ward *et. al.*[21] to afford the three inhibitors. The ruthenium complexes [**1**]Cl_2-[**6**]Cl_2 were then synthesized by coordination of each inhibitor or pyridine to the precursor complexes [Ru(tpy)(NN)Cl)]Cl in the presence of $AgPF_6$. The ruthenium compounds were then isolated as chloride salts by salt metathesis to ensure water solubility. Single crystals suitable for X-ray analysis were grown of [**6**]$(OTf)_2(H_2O)$

(MeOH)(Et_2O). The resolved structure is shown in Figure 2; a selection of bond lengths and angles is reported in Appendix table SIII.1

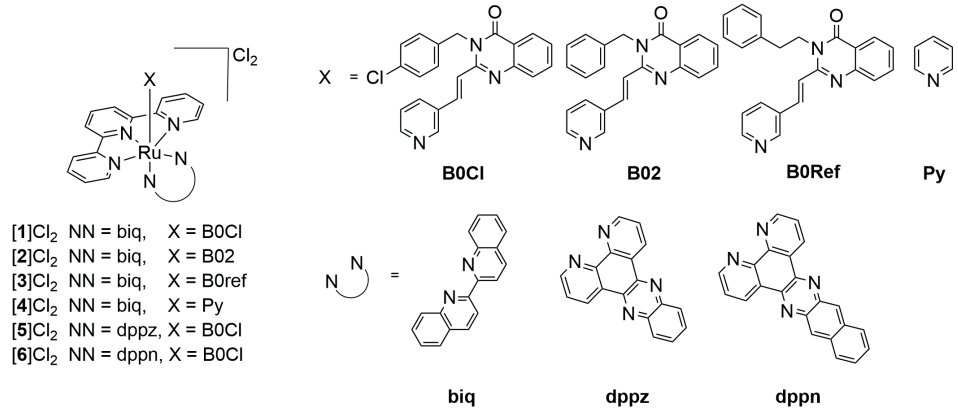

Figure 1. Overview of the ruthenium-photocaged RAD51 inhibitors synthesized in this study.

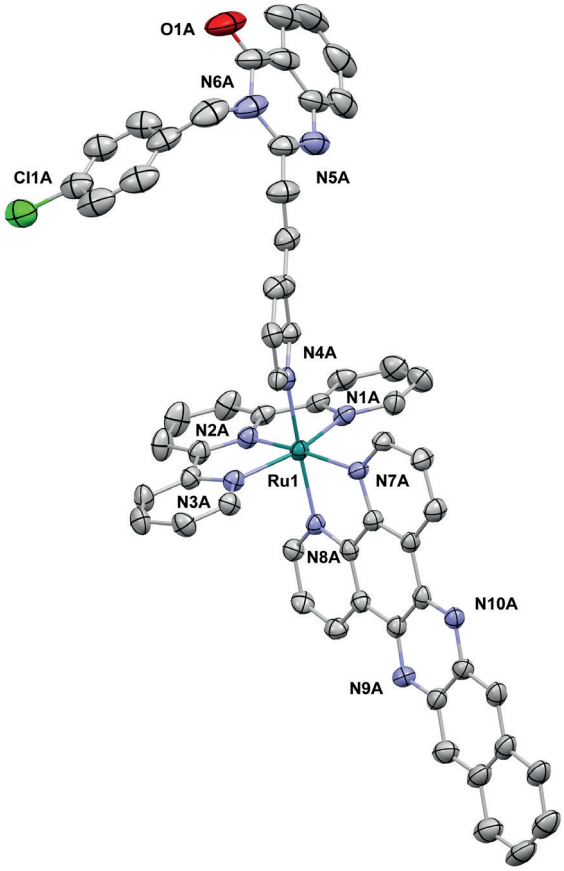

Figure 2. Displacement ellipsoid plot (50% probability level) of $[\mathbf{6}]^{2+}$ in the crystal structure of $[\mathbf{6}](OTf)_2(H_2O)(MeOH)(Et_2O)$. Counter ions, solvent molecules and hydrogen atoms have been omitted for clarity.

4.3 Photochemical characterization

The photophysical properties of compounds [**1**]Cl_2-[**6**]Cl_2 are shown in Figure 2 and Table 1. The UV-vis spectra of complexes [**1**]Cl_2-[**4**]Cl_2 were found to be almost identical and are characterized by an absorbance maximum at 530 nm with molar extinction coefficients of around $8 \cdot 10^2$ $M^{-1}cm^{-1}$. Compounds [**5**]Cl_2 and [**6**]Cl_2 show absorption maxima at a lower wavelength (472 nm) but with higher molar extinction coefficient (~$1.3 \cdot 10^3$ $M^{-1}cm^{-1}$). The photosubstitution of pyridine or of the pyridine-based inhibitor by [**1**]Cl_2-[**6**]Cl_2 was studied upon green light irradiation (505 nm) in MeCN. The time evolution of the UV-vis spectra of solutions of [**1**]Cl_2 and [**4**]Cl_2 are shown in figure 3c and 3d, respectively. The spectra for the other complexes can be found in appendix figure SIII.1. For complexes [**1**]Cl_2-[**4**]Cl_2 the time evolution of the absorption spectra are characterized by multiple isobestic points, indicating the presence of only 2 distinct species interconverting in a single-step photoreaction. Mass spectrometry (MS) measurements allowed identification of the photoproduct as $[Ru(tpy)(biq)(Cl)]^{1+}$ for all four compounds (appendix figure SIII.2). Furthermore, UV-vis control experiments of the complexes in the dark showed no reaction, which confirmed that the photosubstitution reaction only occurred upon light irradiation. These measurements allowed the determination of the quantum yields for ligand substitution (Table 1). The photosubstitution quantum yields of [**1**]Cl_2-[**3**]Cl_2 are around 0.06, while the quantum yield for the pyridine compound [**4**]Cl_2 is slightly lower (0.04) and in line with the literature value of 0.03.[26] The photosubstitution quantum yields for compound [**1**]Cl_2-[**4**]Cl_2 are similar as structural and electronic differences are minimal between the compounds bearing either pyridine or one of the three inhibitors. The UV-vis spectra of complexes [**5**]Cl_2, [**6**]Cl_2 in acetonitrile showed minimal changes upon blue light (435 nm) irradiation and quantum yields could not be accurately determined due to evaporation of the solvent at long timescales, even with temperature control set at 25 °C.

Table 1. Photochemical characterization of compounds [**1**]Cl_2-[**6**]Cl_2 in MeCN and T = 295 K, including molar extinction coefficients (ε), quantum yields of photosubstition (φ_s), and singlet oxygen quantum yields (φ_Δ), where φ_Δ is determined by 1270 nm emission.

Compound	λ_{max} (nm)	ε at λ_{max} ($M^{-1}cm^{-1}$)	φ_s	φ_Δ
[**1**]Cl_2	530	$7.8 \cdot 10^2$	$6.3 \pm 0.1 \cdot 10^{-2}$	0.05
[**2**]Cl_2	530	$8.4 \cdot 10^2$	$6.2 \pm 0.1 \cdot 10^{-2}$	<0.01
[**3**]Cl_2	530	$8.9 \cdot 10^2$	$6.5 \pm 0.3 \cdot 10^{-2}$	<0.01
[**4**]Cl_2	530	$6.9 \cdot 10^2$	$4.3 \pm 0.2 \cdot 10^{-2}$	<0.01
[**5**]Cl_2	472	$1.2 \cdot 10^3$	$<10^{-4}$	0.04
[**6**]Cl_2	476	$1.4 \cdot 10^3$	$<10^{-4}$	0.85

The decrease of the photoreactivity, compared to compounds based on NN = biq, can be explained by the nature of the bidentate ligand. $[Ru(tpy)(NN)(py)]^{2+}$ compounds bearing a NN=biq chelate have been shown to undergo efficient photosubstition of pyridine monodentate ligands. The biq ligand enforces high steric strain in compounds [**1**]Cl_2-[**4**]Cl_2, which lowers ^{3}MC states necessary for photosubstitution to occur.[27] Meanwhile, their dppz and dppn analogues are photoinert,[28] which is attributed on the one hand to the absence of steric strain, and on the other hand to the extended aromatic size of the dppn ligand that generates low-lying $^3\pi\pi^*$ states that quench the ^{3}MC states.[26] Ruthenium complexes bearing the dppn ligand are hence unsuitable for photosubstitution but are established as potent singlet oxygen producers upon light irradiation, as $^3\pi\pi^*$ excited states are typically long-lived.[29] The singlet oxygen production was therefore determined upon excitation by blue light (450 nm) for complex [**1**]Cl_2, [**5**]Cl_2 and [**6**]Cl_2. Only the dppn compound [**6**]Cl_2 shows a strong emission peak at 1270 nm characterized by a $^1O_2$ generation quantum yield of 85%, demonstrating its potential as a PDT agent. The two other compounds do not show any significant $^1O_2$ production, rendering them incapable of inducing any photodynamic therapy (PDT) effect. Overall, the photosubstitution of compounds [**1**]Cl_2-[**4**]Cl_2 demonstrated excellent suitability of these four complexes for PACT. Compound [**5**]Cl_2 is inert upon light irradiation and hence suitable neither for PACT nor PDT, while compound [**6**]Cl_2 is a potential PDT agent, demonstrating $^1O_2$ generation, but minimal photosubstitution, limiting its PACT potential.

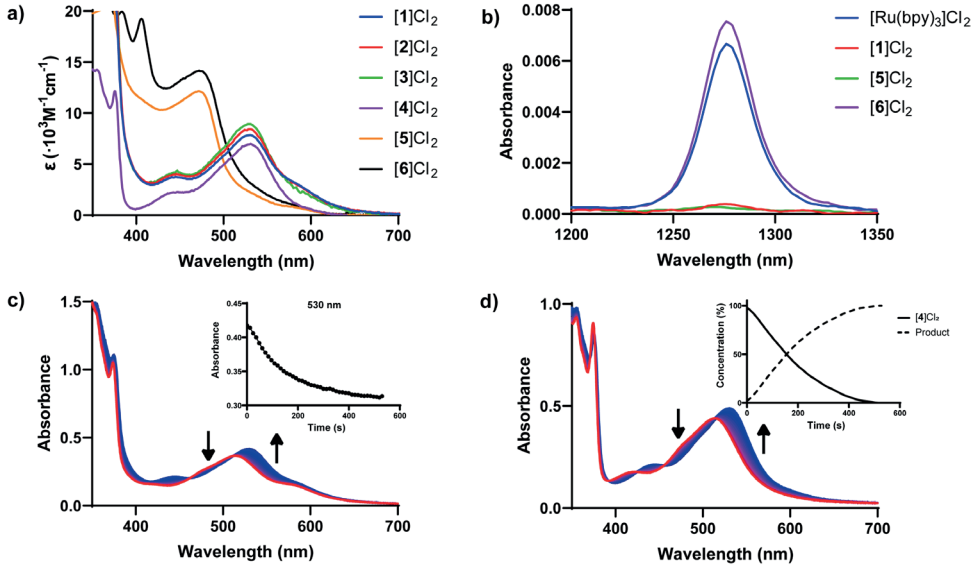

Figure 3. a) Molar extinction coefficients of complexes [**1**]Cl_2-[**6**]Cl_2 in MeCN . b) Singlet oxygen emission at 1270 nm under blue light irradiation of $[Ru(bpy)_3]Cl_2$, [**1**]Cl_2, [**5**]Cl_2, and [**6**]Cl_2. c) Time evolution of the absorbance spectrum of compound [**1**]Cl_2 in MeCN (51 µM) upon green light (520 nm) irradiation, photon flux $5.7{\cdot}10^{-9}$ mol s^{-1}, T = 295 K. Inset shows the absorbance at 530 nm over time. d) Time evolution of the absorbance spectrum of compound [**4**]Cl_2 in MeCN (59 µM) under green light (520 nm) irradiation, photon flux $5.7{\cdot}10^{-9}$ mol s^{-1}, T = 295 K. Inset shows concentration evolution of [**4**]Cl_2 and the photoproduct over time.

4.4 RAD51 expression and cytotoxicity

To test the biological properties of compounds [**1**]Cl_2-[**6**]Cl_2, we selected metastatic liver uveal melanoma cell lines OMM2.5 and MM66. First, the expression of RAD51 was examined by Western blot for both uveal melanoma cell lines OMM2.5 and MM66 under normoxic (21% O_2) and hypoxic (1% O_2) conditions as well as for MCF7, a breast cancer line under normoxic conditions (Figure 4). All conditions resulted in comparable protein levels, although the hypoxic cell lines appear to show slightly lower ratios of RAD51/β-Actin. This could be in the margin of error and the experiment should be repeated for accuracy. Suppression of homologous recombination is documented in the literature for other cell lines under hypoxic conditions.[30] In a second step, a 3-(4,5-dimethylthiazol-2-yl)-2,5-diphenyl-2H-tetrazolium bromide (MTT) cytotoxicity study of the three individual RAD51 inhibitors B0Cl, B02 and B0Ref was performed (Table 2). For this assay, the cells were seeded at t=0, treated with the free RAD51 inhibitors at 24 h, and, finally, the relative cell population was measured after 72 h incubation. As expected, the improved inhibitor B0Cl induced the highest toxicity, with EC50 values of 5.4 µM in OMM2.5 and 3.1 µM in MM66, which are comparable to the values reported by Ward *et al.* for several triple-negative breast cancer cell lines.[21] The two inhibitors B02 and B0Ref show slightly lower cytotoxicity. B0Ref was initially included as a negative control that should show minimal RAD51 inhibition, but the similar toxicity compared with B0Cl renders B0Ref unsuitable for that purpose. It remains unknown whether the toxicity of B0Ref in these cell lines is induced by the inhibition of RAD51 or by another mechanism. Compound [**3**]Cl_2, containing the caged inhibitor B0Ref, is therefore omitted from further biological testing.

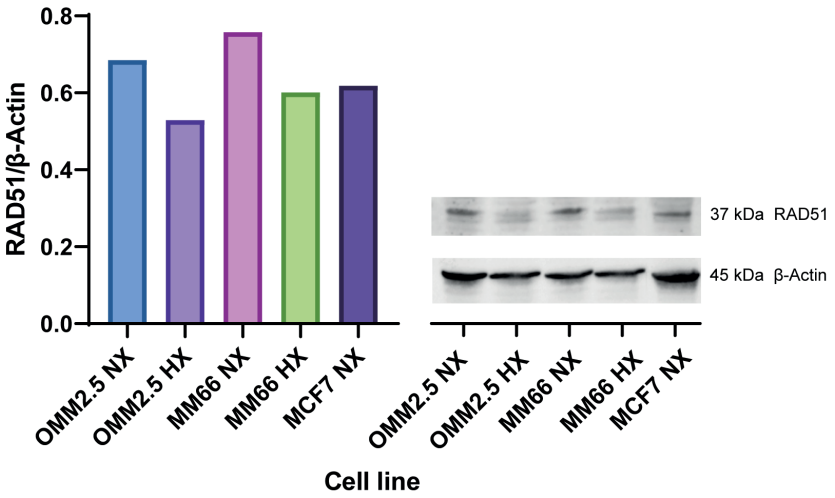

Figure 4. The ratio of black value intensities from RAD51 and β-actin Western blot. RAD51 and β-Actin protein levels were measured in OMM2.5, MM66 and MCF7 cell lines under normoxic (NX) and hypoxic (HX) conditions. The graph illustrates data from a single experiment, and as such, there are no error bars included to represent variability or uncertainty in the measurements.

Table 2. MMT cytotoxicity study of the three inhibitors B0Cl, B02, and B0Ref.

Cell line	B0Cl		B02		B0Ref	
	EC_{50} (μM)	Cl (95%)	EC_{50} (μM)	Cl (95%)	EC_{50} (μM)	Cl (95%)
OMM2.5	5.4	+6.1 -5.2	>11	+ -10	17	+5.3 -4.4
MM66	3.1	+5.1 -2.9	>3.4	+ -	>14	+6.2 -

4.5 Phototoxicity and uptake

The phototoxicity of compounds [**1**]Cl_2, [**2**]Cl_2 and [**4**]Cl_2 was studied following the same MTT assay as above in both normoxic (21% O_2) and hypoxic (1% O_2) conditions for UV melanoma cell lines OMM2.5 and MM66. The cells were seeded at t=0, treated with the compounds at t = 24 h and at 48 h the cells were washed and exposed to green light (13.1 J/cm^2, 15 min) to achieve light activation. The end-point viability assay was realized at t = 96 h. EC_{50} values are given in Table 3. In normoxia, compound [**1**]Cl_2 shows the highest light-activated toxicity with values of 2.7 μM for OMM2.5 and 3.5 μM for MM66 and photoindexes (PI) defined as $EC_{50,dark}$ / $EC_{50,light}$, of 2.7 and 3.3, respectively. The same trend is seen for B02 compound [**2**]Cl_2 while pyridine compound [**4**]Cl_2 is strikingly less toxic, with light-activated EC_{50} values of 46.8 μM for OMM2.5 and 47.5 μM for MM66 and dark EC_{50} values above 100 μM. The light-activated cytotoxicity of [**1**]Cl_2 is similar to that of the free B0Cl inhibitor. This result suggests that the cytotoxicity of light-activated [**1**]Cl_2 is mainly induced by the uncaged inhibitor B0Cl and that the contribution of the uncaged metal complex is minimal. Under hypoxia, the cytotoxicity after light activation is slightly lower for all compounds and cell lines, while the dark toxicity did not change much, leading to lower PI values. Increased resilience is commonly reported for hypoxic cells, not only for oxygen-based PDT treatments, for which the PI values can typically be 1 or 2 orders of magnitude lower,[31–33] but also for non-light activated chemotherapy.[34] The relatively small difference in light toxicity observed here between normoxic and hypoxic conditions and the low $^1O_2$ generation quantum yields reported above suggest an oxygen-free mechanism of action. However, the low PI values for compound [**1**]Cl_2 and [**2**]Cl_2 renders them unsuitable for PACT treatment under hypoxic conditions, at least as monotherapy.

The difference in dark toxicity between compound [**1**]Cl_2 and [**4**]Cl_2 is remarkable. One factor to take into consideration could be the cellular uptake of these compounds. The B0Cl inhibitor in compound [**1**]Cl_2 increases the lipophilicity of the ruthenium conjugate significantly, compared with the pyridine ligand in complex [**4**]Cl_2. This effect was quantified by a cellular uptake study in OMM2.5 cell line following 24 h incubation with either compound. To do so, the number of cells was determined by a Hoechst stain followed by cell counting using confocal imaging, after which the

intracellular ruthenium concentration was measured using Inductively Coupled Plasma Mass Spectrometry (ICP-MS). The uptake for compound [**1**]Cl_2 and [**4**]Cl_2 are 0.39 ng Ru/10^6cells and 0.12 ng Ru/10^6 cells, respectively. Even though the uptake of [**1**]Cl_2 exceeds the uptake of [**4**]Cl_2 by a factor 3, it does not fully account for the difference in dark cytotoxicity between these two compounds. While the uptake and lipophilicity, at least, partly affect the cytotoxicity, these results suggest that the main contribution to the toxicity of these complexes is likely the higher biological activity of the B0Cl inhibitor, in comparison with pyridine.

Table 3. Cytotoxicity of compounds [**1**]Cl_2, [**2**]Cl_2 and [**4**]Cl_2 under normoxic and hypoxic conditions.

			[**1**]Cl_2			[**2**]Cl_2			[**4**]Cl_2		
Cell line	O_2 (%)	Light	EC_{50} (μM)	Cl (95%)	PI[1]	EC_{50} (μM)	Cl (95%)	PI	EC_{50} (μM)	Cl (95%)	PI
OMM2.5	21	Dark	7.5	+1.9 -1.7	2.7	15	+3.6 -2.9	2.1	>100	-	>2.1
		Light	2.7	+2.4 -1.6		6.7	+1.3 -1.2		46.8	+16.4 -12.8	
	1	Dark	15	+2 -2	1.9	17	+14 -7	1.4	>100	-	-
		Light	7.9	+1.3 -1.2		12	+6.0 -4.4		>100	-	
MM66	21	Dark	10	+2.7 -2.2	3.3	13	+7.1 -4.2	2.2	>100	-	>2.1
		Light	3.5	+0.8 -0.7		5.7	+2.1 -1.7		47.5	+12.1 -9.9	
	1	Dark	11	+1.9 -1.6	1.0	16	+5.4 -4.0	1.6	>100	-	>1.7
		Light	11	+1.9 -1.5		10	+2.8 -2.3		60.2	+20.4 -13.4	

[1] PI = $EC_{50,dark}$ / $EC_{50,light}$. Experimental errors are calculated based on three technical replicates, repeated in three independent biological replicates.

4.6 γH2AX imaging of OMM2.5 cells

According to the previous data, the phototoxicity of [**1**]Cl_2 and [**2**]Cl_2 is likely linked to RAD51 inhibition following light irradiation. The amount of unrepaired double-strand breaks (DSBs) should therefore increase in cells upon light activation. To study the presence of DSBs in treated cells, OMM2.5 cells were treated with 10 μM of compound [**1**]Cl_2, [**2**]Cl_2 or [**4**]Cl_2 or 500 nM doxorubicin at t = 48, light activated at t = 72 h, stained with the commonly used DSB marker γH2AX, fixed, and finally imaged at t = 78 h (Figure 5). Light activation of compounds [**1**]Cl_2 and [**2**]Cl_2 shows an increase in fluorescence in comparison to dark controls and vehicle control, while the light activation of [**4**]Cl_2 shows a minimal increase in fluorescence compared to dark control. However, the difference in intensity of γH2AX foci is small and would require better quantification and more replicates. The increase in DSB observed for compounds [**1**]Cl_2 and [**2**]Cl_2 may result from naturally occurring DBSs that accumulate upon inhibition of RAD51 and homologous recombination. Another explanation for the increased γH2AX foci is

the potential interaction of the uncaged metal species with DNA, which may result in the formation of DSBs. Metal complexes that interact and damage DNA are well-documented in the literature.[35,36] On the other hand, the increase in luminescence upon activation of [**4**]Cl_2 is very small in comparison with the γH2AX foci observed upon treatment with doxorubicin, which is a powerful DSB inducer. These results show that photoactivation of the ruthenium conjugates did result in DSB accumulation, albeit at a lower scale than that induced by Dox. Considering the margin of error these results should be repeated and better quantified.

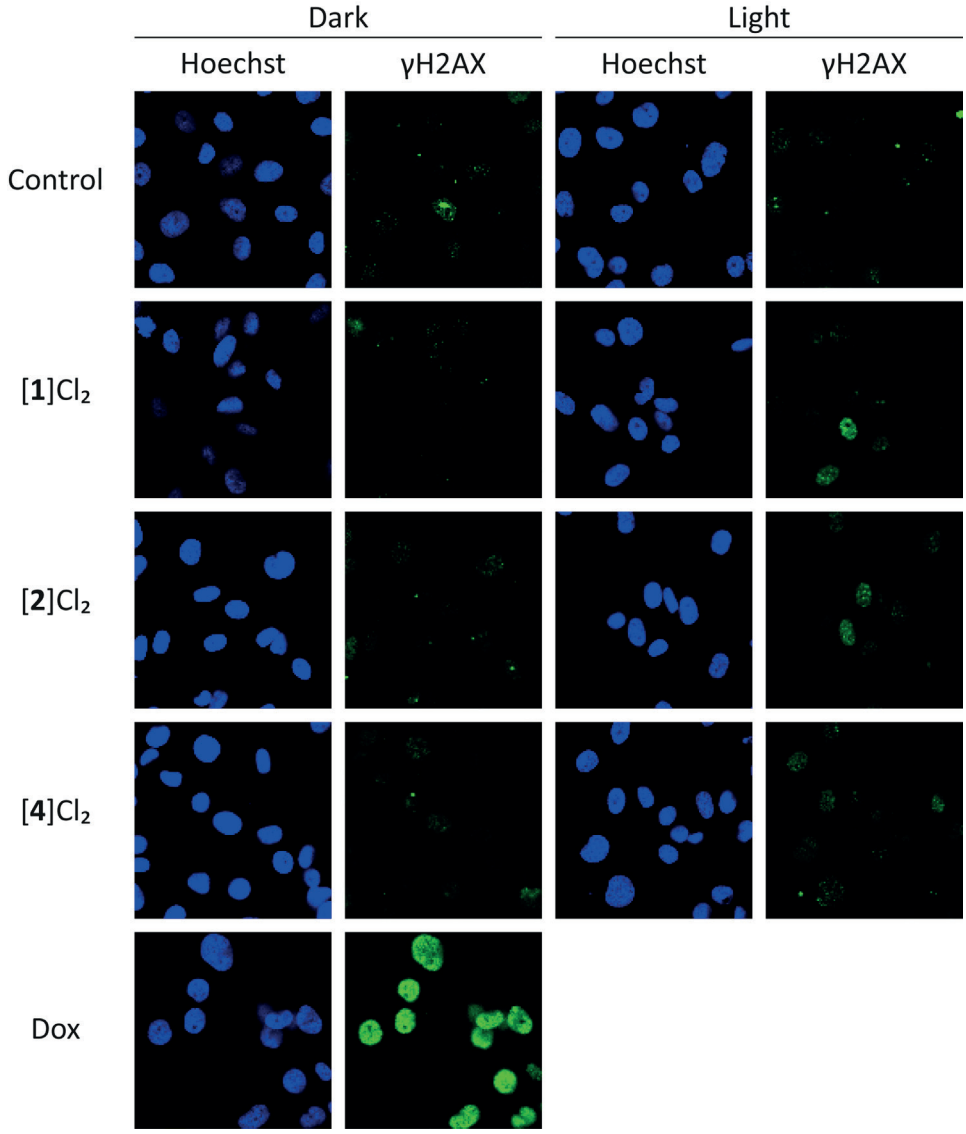

Figure 5. Immunofluorescence γH2AX foci images of OMM2.5 cells treated with 10 μM of compound [**1**]Cl_2, [**2**]Cl_2, [**3**]Cl_2 or 500 nM Dox in the dark and photoactivated by 15 min of green light (13.1 J/cm^2). Blue shows the nuclei (Hoechst staining).

4.7 Dox and RAD51 inhibitor

As the phototoxicity of [**1**]Cl_2 appears to be mainly induced by the released inhibitor, we considered treating the cancer cells with a combination of Dox and [**1**]Cl_2. The synergistic effects between Dox and RAD51 inhibition is a widely explored topic in the literature.[20] Photoactivation of the inhibitor could offer increased selectivity of a systemic Dox treatment by local light irradiation. To do so, we conceived an experiment where MM66 cells were treated with complex [**1**]Cl_2 (10 µM) at t=24 h, irradiated by light after media refreshing at 48 h or kept it in the dark, further treated with Dox at t=54 h (500 nM), incubated until t=78 h in the dark, and finally imaged by confocal microscopy (figure 6). The idea was to image both γH2AX foci and RAD51 foci. During the repair of DSBs by homologous recombination, RAD51 accumulates at the break side and forms a nucleofilament with DNA. Imaging RAD51 foci can therefore be used as a marker for homologous recombination repair of DSBs, while γH2AX foci show, as discussed above, the DSB themselves.

Upon treatment of the cells with only Dox, both the γH2AX and RAD51 foci increased substantially in comparison with the untreated control, showing that the amount of DSB increased as well as that of HR repair. A similar observation is seen for cells treated with a combination of Dox and [**1**]Cl_2 in the dark, indicating compound [**1**]Cl_2 is inert in the dark with respect to HR activity. However, upon light activation, the RAD51 foci decreased, while the amount of γH2AX foci remained similar. Qualitatively, the apparent decrease of HR activity indicated the successful light activation of compound [**1**]Cl_2 and release of the RAD51 inhibitor B0Cl. On the other hand, the observed differences were small and might be within the margin of error; this preliminary experiment should therefore be repeated for better quantification. This experiment should also be repeated with cell lines with increased RAD51 expression. However, these initial tests demonstrate that the B0Cl inhibitor is successfully caged in [**1**]Cl_2, and that it can be released by light activation in cells to reduce HR activity.

To study the consequences of RAD51 inhibition in cells treated with Dox the combination treatment of [**1**]Cl_2 and Dox was further explored by an apoptosis experiment using flow cytometry Fluorescence-Activated Cell Sorting (FACS) analysis and a double staining with Annexin V and Propidium Iodide (PI). Annexin V binds to early (quadrant Q2) or late (quadrant Q3) apoptotic cells while PI stains cells that die via necrosis (quadrants Q3 and Q4), while alive cells are both Annexing V and PI negative (quadrant Q1) In this assay, the percentage of apoptotic cells were determined by the combination of the two right quadrants (Q2, Q3); the corresponding data is shown in Figure 7. The number of cells undergoing apoptosis increased slightly (2.5% for OMM2.5 cells and 2.83% MM66 cells) upon treatment with Dox alone at this concentration, or in combination with [**1**]Cl_2 in the dark. Upon light irradiation, these numbers increased substantially to 14.0 % for OMM2.5 cells and 6.1 % for MM66 cells. The total amount of apoptosis in

both cell lines remained low, which is attributed to the short incubation time after light irradiation (24 h) necessary to quantify apoptotic cell death by FACS. However, these results suggest that photoactivation of the inhibitor directly resulted in apoptotic cell death.

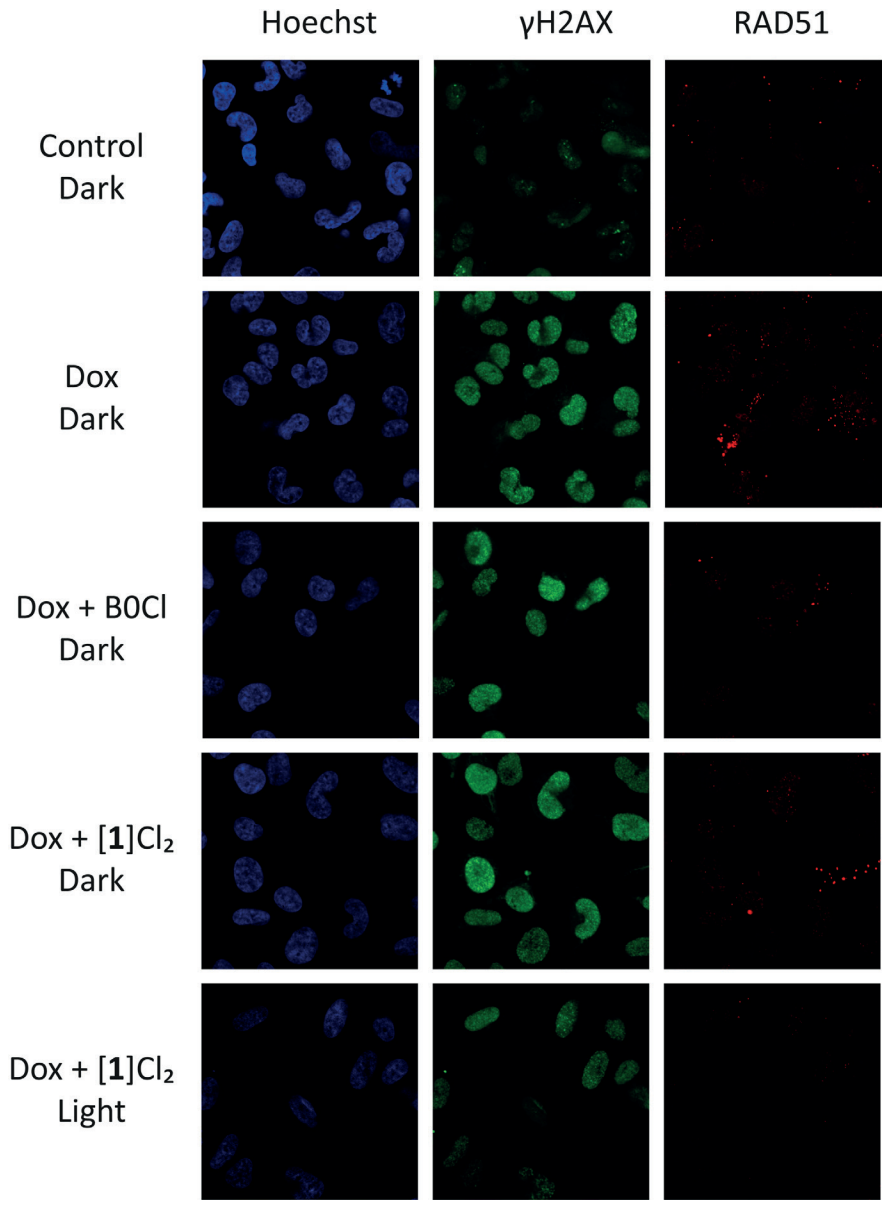

Figure 6. Immunofluorescence Hoechst, γH2AX, and RAD51 staining of HM66 cell treated with 10 µM of B0Cl or [**1**]Cl_2 and or 500 nM of Dox in the dark and upon photoactivation by 15 min of green light irradiation (13.1 J/cm^2).

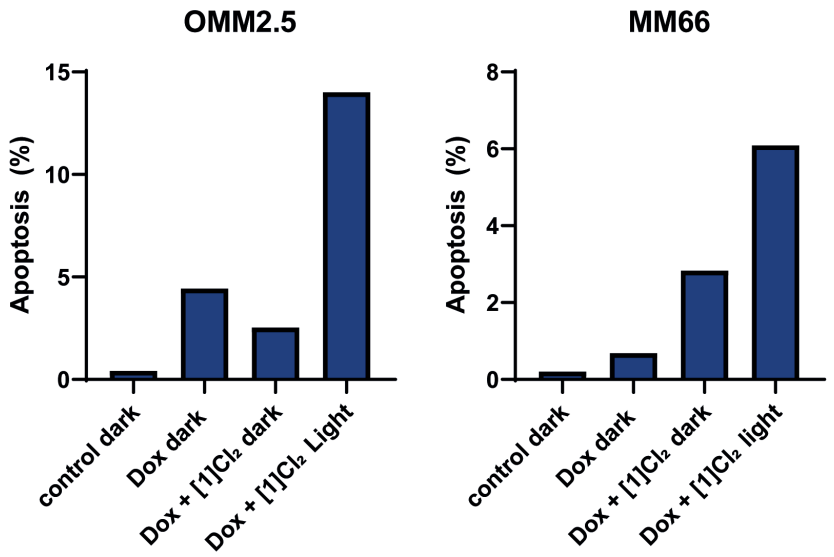

Figure 7. Quantification of apoptosis by FACS in OMM2.5 and MM66 cells co-treated with [**1**]Cl_2 and Dox using Annexin V and Propidium Iodide (PI) staining. The percentage of apoptotic cells is determined by the combination of the two right quadrants (Q2, Q3). Irradiation conditions: 15 min of green light (13,1 J/cm2).

4.8 Discussion

The combination treatment of cancers using a DNA damage inducer and an inhibitor of the corresponding DNA repair pathway has been widely discussed in the literature.[37] However, creating combinations is not as clear cut as it initially appears to be. DNA damage agents can induce different kinds of chemical damage, while the DNA repair pathways overlap substantially. The widely explored DNA damage inducer cisplatin, for instance, is well known for primarily generating (90%) intrastrand crosslinks,[38] but also form a minor amount (1–3%) of interstrand cross-links (ICLs).[39] Distinct molecular mechanisms are required for the repair of both types of adducts[40]. Intrastrand DNA crosslinks are primarily repaired by nucleotide excision repair (NER) [13,41] while ICLs are mostly repaired by the Fanconi's Anemia pathway (FA), enlisting elements of NER, homologous recombination (HR), and mutagenic translation synthesis.[42] Furthermore, the repair of platinum-induced lesions have also been linked to mismatch repair (MMR), base excision repair (BER), HR, and non-homologous end joining (NHEJ).[43] Experimentally speaking, inhibiting the NER,[44,45] HR,[30,46,47] NHEJ,[48,49] or FA[50,51] pathways has been reported to sensitize cells to cisplatin treatment.

Dox is comparatively simpler, with two main mechanisms of action: (I) free radical formation and induction of oxidative damages,[52] (II) intercalation into DNA and subsequent binding to DNA replication and transcription proteins, such as topoisomerase I & II, mostly resulting in the formation of DSBs.[53] Inhibition of the DSB repair pathways (HR[19,20] and NHEJ[54,55]) has been reported to sensitize cells to Dox

treatment, and combination therapies are actively explored. A multitude of cancers show mutations in the DNA repair pathways, which could be exploited to enhance tumor selectivity. The potential of this idea is elegantly displayed by selective PARP inhibitors for the treatment of breast tumors bearing the BRCA1/2 mutations.[56] Most DNA repair inhibitors, however, do not provide the same degree of selectivity and effectiveness as PARP inhibitors. Overall, even though combination therapy using inhibitors of the DNA repair pathways with DNA damage inducers is promising and may enhance antitumor treatment at lower chemotherapy doses, the selectivity of such an approach remains limited. Focusing on cancers with well-established mutations in the DNA repair pathway might provide increased selectivity, but there is no guarantee that systemic combination treatments would offer enough selectivity for the sensitization of cancer tissues over healthy tissues, and hence that this strategy will be able to reduce side effects significantly.

A combination approach including a light-activated HR inhibitor offers a new perspective, as the inhibitor would be released only in the cancer cells that have been irradiated with light, and prior to systemic treatment with FDA-approved, DSB-inducer Dox. Non-irradiated (healthy) cells in the rest of the body would keep their ability to repair DSB, while Dox would generate deadly DSB in the cancer tissue. Of course, this approach needs validation *in vivo*, but the results shown here demonstrate *in vitro* that it is possible to control the activity of the RAD51 inhibitor B0Cl by photocaging it by a ruthenium scaffold: in the dark, the activity of the inhibitor is quenched, while irradiation by green light re-activates it.

4.9 Conclusion

The synthesis and full photochemical characterization of 5 novel ruthenium-based conjugates of RAD51 inhibitors is reported. The photosubstitution quantum yields of the sterically strained compounds [**1**]Cl_2-[**3**]Cl_2 are all around ~0.06, which is excellently suited for PACT treatment of cancer. Compound [**4**]Cl_2, their pyridine analogue, was chemically speaking also activated by light, but its biological activity was minimal even after light activation, thus showing the minor role of ruthenium itself in the activated toxicity of [**1**]Cl_2-[**3**]Cl_2. Without the steric strain induced by the biq ligand, compounds [**5**]Cl_2 and [**6**]Cl_2 showed negligible photosubstitution quantum yields. [**6**]Cl_2 has excellent potential as PDT agent with a singlet oxygen generation quantum yield of 0.85, while [**5**]Cl_2 could neither generate $^1O_2$, nor release the RAD51 inhibitor. *In vitro* [**1**]Cl_2 showed the highest light-activated cytotoxicity with EC_{50} of 2.7 µM and 3.3 µM for cell lines OMM2.5 and MM66, respectively, though the significant dark toxicity suggests another mode of cytotoxic action for this compound. Immunofluorescence staining showed a small increase of γH2AX foci upon light activation of [**1**]Cl_2, but this increase was minimal in comparison with that brought about by Dox. The highest potential of these ruthenium compounds appeared to be in combination therapy.

When combining treatment with [**1**]Cl_2 and Dox, an increase of γH2AX and RAD51 foci in the dark was observed due to the non-inhibited repair action of the Dox-induced DSB. Light activation led to a decrease of the RAD51 foci but a similar amount of γH2AX foci, which is consistent with the photorelease of the B0Cl RAD51 inhibitor. This kind of compounds might be used to sensitize a tumor to Dox by local light irradiation, which may be used to decrease side effects during chemotherapy treatment with Dox.

4.10 Experimental

4.10.1 General

[Ru(tpy)(biq)Cl]Cl,[1] [Ru(tpy)(dppz)Cl]Cl[57] and [Ru(tpy)(dppn)Cl]Cl[26] were prepared according literature procedures. Size exclusion columns were prepared by soaking Sephadex LH-20 overnight in an excess of methanol. The suspension was poured in a class column tube with a diameter of 3 cm and the excess of methanol was drained out, leaving a final column length of 100 cm. NMR spectra were recorded on a Bruker AV-500, AV-600, or AV-850 spectrometers. High-resolution mass spectra (HRMS) were recorded on Waters XEVO-G2 XSQ-TOF) mass spectrometer equipped with an electrospray ion source in positive mode (source voltage 3.0 kV, desolvation gas flow 900 L/hr, temperature 250 °C) with resolution R= 22000 (mass range m/z = 50-2000) and 200 pg/uL Leu-enkephalin (m/z = 556.2771) as a "lock mass". The human metastatic uveal melanoma cell lines OMM2.5 and MM66 were cultured in Dulbecco's modified eagle medium (DMEM-F12) (Sigma) serum containing 10% FCS, 100 U/mL of penicillin, and 100 µg/mL of streptomycin and glutamax. The cells were maintained at 37°C, 5% CO_2. For the hypoxic cell cultures, cells were incubated in the hypoxia incubator at 1% O_2 for at least 2 weeks prior to the experiment. All treatments were dissolved in DMSO and diluted in Opti-MEM reduced FCS cell culture medium (Gibco) before using them. Doxorubicin was purchased from Medchemexpress.

4.10.2 Photochemistry

Singlet oxygen quantum yields were determined following a literature method.[58] Substitution quantum yields were determined on an Agilent Technologies Cary 60 UV-vis spectrometer. 3.00 mL of a solution of [**1**]Cl_2-[**6**]Cl_2 in MeCN (~10^{-5} M) was put in a 1 cm optical pathway cuvette and deoxygenated by bubbling N_2 for 5 min while stirring with a magnetic bar. The solution was then radiated from above with a 505 nm monochromatic LED. The photon flux was determined by ferrioxalate actinometry.[59] Both the cuvette and the LED were temperature-controlled at 25°C and absorption spectra were recorded every 12 sec for 20 min. Quantum yields were then determined by the two wavelength method described in the literature.[60] Dark controls were measured in a similar experimental setup, but without the light irradiation. Spectra were recorded every 1 min for 30 min.

4.10.3 MTT assay

For the measurement of the cytotoxicity of the compounds, relative cell viability in presence of different concentration of the compounds was determined by a colorimetric MTT end-point assay. OMM2.5 and MM66 cells were seeded in a 96-well plate at ~6k cells/well at t = 0. At t = 24 h cells were treated with the compound at a concentration ranging from 0.1 to 100 µM. At t = 48 h the medium in each well was refreshed to remove the excess compound, and the well plate was either irradiated with light for 15 min at 520 nm (13,1 J/cm^2), or left in the dark. An MTT (3-(4,5-dimethylthiazol-2-yl)-2,5-diphenyltetrazolium bromide) solution was prepared by dissolving 5 mg/mL MTT (as yellow powder) in PBS (Sigma). At t = 96 h, 10 µL of this MTT solution was added to each well, and the plate was incubated further for 3 h at 37 °C, before the solvent was removed by turning the plate upside down. The purple Formazan crystal was then solubilized in DMSO (200 µL), and absorbance was measured at 570 nm using a Tecan reader. All experiments were conducted in independent biological triplicate. The obtained data were analyzed with Graphpad Prism 5 using the dose–response two-parameter Hill slope equation (eq 1) to obtain the half-maximal effective concentrations EC_{50} (defined as the concentration of drug that kills 50% of cells, compared to the untreated control).

$$100/(1 + 10^{((log_{10} Ec_{50} - X) Hill\ Slope)})$$

4.10.4 Uptake

OMM2.4 or MM66 Cells were seeded in a 96-well plate at a density of ~ 6k cells per well at t =0 h. At t = 24 h cells were treated with the compounds all at a concentration of 5 µM. At t = 48 h cells were stained for cell counting as follows: After washing once with PBS cells were incubated with Nucblue (Invitrogen) staining for 25 min. The nuclei were then imaged using a Nikon confocal microscope and counted with the ImagePro 7.0 program to measure the number of cells in each well. After imaging, the cells were lysed with 65% HNO_3 for 30 min at room temperature. The cell lysates were then moved to a deep well plate (Eppendorf, E951033502) and diluted 20x with MilliQ water to achieve a final HNO_3 concentration of ~3%. The plate was sealed with foil and stored at 4 °C. Lastly, ruthenium concentration was measured using ICP-MS S (NexION 2000, PerkinElmer) and final ruthenium concentrations were determined in ppb (µg/L).

4.10.5 Immunofluorescence

Cells were seeded in a 96-well plate at ~12k cells/well. For the monotreatment in OMM2.5 cell, the cells were treated with 10 µM of compound [**1**]Cl_2, [**2**]Cl_2 or [**4**]Cl_2 or 500 nM doxorubicin at t = 48, light activated at t = 72 h, incubated until t=78 h in the dark. The combination experiments in MM66 cells were also seeded in a 96-well plate

at ~12k cells/well. Treated with complex [**1**]Cl_2 (10 µM) at t=24 h, irradiated by light after media refreshing at 48 h or kept it in the dark, further treated with Dox at t=54 h (500 nM), incubated until t=78 h in the dark.

At t = 78 h the cells were fixed using 4% paraformaldehyde in PBS for 15 min at RT. Cells were washed in PBS with three five-minute washes, permeabilized using 0,3 % Triton X-100 in PBS for 5 min, rinsed in PBS (once, 5 min) and incubated for 1 h at RT with blocking buffer (5% BSA 0,3% Triton X-100 in PBS). Subsequently to blocking, the primary antibody which was diluted in (1% BSA 0,3% Triton X-100 in PBS) (RAD51, #GTX70230 GeneTex d1/300 and/or p-histone H2A.X #2577 Cell Signaling) was added and left overnight at 4°C under mild agitation. Cells were washed 3 times for 5 min with PBS and incubated for 2 h at RT with the corresponding secondary antibody (Anti-rabbit Alexa fluor 488 #4412 Cell signalling d1/1000 and/or Anti-mouse Alexa fluor 647 #4410 Cell signalling d1/1000) and Nucblue (Invitrogen).Plates were stored at 4°C and covered with foil for further imaging.

4.10.6 Confocal Microscopy

Images of the γH2AX and RAD51 foci were acquired using a Ti2 eclipse inverted microscope, with a C2Si confocal system including a spectral detector (Nikon). γH2AX and RAD51 foci were monitored at 1 Z-stack per timepoint and excited at wavelengths of 409 nm (Hoechst), 489 nm (γH2AX) and 638 nm (RAD51) respectively. Detection bandwidths were set at 430-496 nm in the blue channel (Hoechst), 510-590 nm for the green channel (γH2AX) and 648-720 nm for the red channel (RAD51). Zoom was created using a Apo LWD 40x Water objective with a numerical aperture of 1.15 and a working distance of 0.61–0.59 mm. Pinhole size was set to 30 µm. 10 images were taken of each well. The images obtained were 1024 x 1024 pixels in size representing 0.13 µm/px. The images of the nuclei for the cellular uptake experiment were taken using a Nikon Ti eclipse inverted microscope, with an Intensilight C-HGFIE light source (Nikon) at an excitation wavelength of 409 nm (Hoechst). The objective used was a Plan Fluor 10x air objective with a numerical aperture of 0.3 and working distance of 16 mm. Both microscopes were controlled using the NIS elements software (Nikon).

4.10.7 Western blot

Cells were seeded at 175k cells per well in a 6-well plate or at 450k cells in a 25 cm^2 flask. Cells were lysed at 4 °C by scratching in RIPA buffer (Sigma) plus protease inhibitors (#5872 Cell Signaling). The cell suspension was then centrifuged for 20 min at 13k rpm and supernatants were collected. The protein concentrations of the samples were assessed using a BCA Bradford assay. 17 µg of protein was loaded into each well of a 6-18 % gradient gel (Biorad). The SDS-PAGE was run at 100V for about 1 h. Proteins were then transferred onto a polyvinyl difluoride (PVDF) membrane using the turbo-blot transfer system from Biorad. Membranes were blocked in 5% BSA in TBS-T 0,1%

for 1 h at RT under agitation and afterward probed with primary antibody (p-γH2AX: Cell signalling #2577S d1/2000, or RAD51: #GTX70230 GeneTex d1/1000) overnight at 4 °C on the roller-shaker. Membranes were washed 5 x 5 min in TBS-T, incubated with corresponding secondary antibody HRP-conjugated anti-rabbit IgG (#7074 Cell signalling d1/1000) or HRP-conjugated anti-mouse IgG (#7076 Cell signalling) for 1 h at RT, washed again, and the signal was detected using chemiluminescence ECL detection reagent (Biorad). The membrane was stripped of the antibodies by washing 3 x 20 min and reprobed for Beta actin (#4967 Cell signalling d1/1000) as described above. Bands were quantified using ImageJ software and each lane was expressed relative to the beta-actin band and control condition.

4.10.8 Apoptosis assay using FACS

Cells were seeded at t = 0 h with a density of 175k cells per well in a 6-well plate. The cells were treated at t = 24 h with compound [**1**]Cl_2 followed by Dox (500 nM) at t = 48 h and were light activated by green light (520 nm). At t = 72 h the cells were prepared for FACS analysis. The supernatant and the cells were harvested after trysinisation from the 6-well plates, centrifuged for 5 min at 1000 rpm at room temperature, resuspended in 1 mL of Opti-MEM and centrifuged again for 5 min at 1000 rpm at room temperature. After removing the supernatant, 100 µL of Annexin V/PI staining was added to the cell pellet. The staining was prepared in 1x Annexin V binding buffer (Exbio EXB0019) containing 1 µL of PI (Exbio EXB0018) and 5 µL of Annexin V staining (Exbio EXB0024) per 100 µL of buffer. After a 30 min incubation the samples were transferred to FACS tubes and filled up with Annexin V binding buffer to a final volume of 500 µL. The machine used was the BD FACS Canto with laser channel FITC for Annexin V (ex; 488 nm, em: 525/50 nm) and APC for PI (ex: 633 nm, em: 660/20 nm)

4.10.9 Synthesis

4.10.9.1 B0Cl

Benzylamine (4.0 mL, 37 mmol) and P_2O_5 (4.1 g) were added to 2-Methyl-4H-3,1-benzoxazin-4-one (5.0 g, 31 mmol) in pyridine (100 mL) and the reaction mixture was stirred overnight at 95 °C. The solvent was removed in vacuo and water (50 mL) and DCM (50 mL) were added to the residue. The layers were separated and the organic layer was dried with magnesium sulfate, filtered and concentrated in vacuo. The crude product was used in the next reaction without further purification.

To this crude was added acetic acid (100 mL), sodium acetate (3.0 g, 37 mmol) and 4-chlorobenzylamine (5.2 g, 37 mmol) and the reaction mixture was stirred overnight at 130 °C under nitrogen atmosphere. The solvent was then removed under vacuo and DCM (50 mL) and 1 M aq. NaOH (50 mL) were added. The layers were separated and the organic layer was dried with magnesium sulfate, filtered and concentrated in vacuo.

Enough DCM was added to dissolve the crude (~10 mL) after which diethylether (200 mL) was added. The mixture was allowed to crystalize overnight at 4 °C, the precipitate was filtered and dried in vacuo to afford the title compound as yellow needles. Yield: 5.2 g 14 mmol, 45 %. Measured spectra were in agreement with those in literature.[21] For information: **^{1}H NMR** (500 MHz, DMSO) δ 8.88 (d, J = 2.2 Hz, 1H), 8.56 (dd, J = 4.8, 1.6 Hz, 1H), 8.19 (dd, J = 7.9, 1.5 Hz, 1H), 8.15 (dt, J = 8.0, 2.0 Hz, 1H), 7.94 – 7.84 (m, 2H), 7.75 (dd, J = 8.3, 1.1 Hz, 1H), 7.55 (ddd, J = 8.1, 7.1, 1.2 Hz, 1H), 7.49 (d, J = 15.5 Hz, 1H), 7.46 (dd, J = 7.8, 4.6 Hz, 1H), 7.38 (d, J = 8.6 Hz, 1H), 7.32 (d, J = 8.6 Hz, 2H), 5.64 (s, 2H). **^{13}C NMR** (126 MHz, DMSO) δ 162.02 (Cq), 152.17 (Cq), 150.89 (CH), 150.10 (CH), 147.58 (Cq), 137.48 (CH), 136.79 (Cq), 135.37 (CH), 134.95 (CH), 132.48 (Cq), 131.37 (Cq), 129.26 (CH), 129.13 (CH), 127.77 (CH), 127.41 (CH), 127.16 (CH), 124.48 (CH), 122.16 (CH), 120.55 (Cq), 45.21 (CH_2). **HR-MS** $[M+H]^+$: 374.10547 (calculated); 374.10522 (measured).

4.10.9.2 B02

Ligand B02 was synthesized according to the procedure for B0Cl. Starting 2-Methyl-4H-3,1-benzoxazin-4-one (31 mmol scale) but with benzylamine instead of 4-chlorobenzylamine to afford the title compound as yellow needles. Yield: 6.4 g 18 mmol, 61 %. Measured spectra were in agreement with those in literature.[21] **^{1}H NMR** (500 MHz, DMSO) δ 8.85 (d, J = 2.1 Hz, 1H), 8.55 (dd, J = 4.7, 1.6 Hz, 1H), 8.20 (dd, J = 8.0, 1.0 Hz, 1H), 8.11 (dt, J = 7.8, 1.8 Hz, 1H), 7.91 – 7.84 (m, 2H), 7.74 (d, J = 7.6 Hz, 0H), 7.55 (ddd, J = 8.1, 7.1, 1.2 Hz, 1H), 7.50 (d, J = 15.4 Hz, 1H), 7.45 (dd, J = 8.6, 4.8 Hz, 1H), 7.35 – 7.26 (m, 4H), 7.27 – 7.20 (m, 1H), 5.66 (s, 2H). **^{13}C NMR** (126 MHz, DMSO) δ 162.05 (Cq), 152.28 (Cq), 150.84 (CH), 150.02 (CH), 147.59 (Cq), 137.77 (CH), 137.23 (CH), 135.31 (CH), 134.87 (CH), 131.41 (Cq), 129.30 (CH), 127.91 (CH), 127.74 (CH), 127.36 (CH), 127.18 (CH), 127.13 (CH), 124.46 (CH), 122.37 (CH), 120.57 (Cq), 45.74 (CH_2). **HR-MS** $[M+H]^+$: 340.14444 (calculated); 340.14433 (measured).

4.10.9.3 B0Ref

Ligand B0Ref was synthesized according to the procedure for B0Cl. Starting 2-Methyl-4H-3,1-benzoxazin-4-one (31 mmol scale) but with phenethylamine instead of 4-chlorobenzylamine to afford the title compound as yellow needles. Yield: 4.6 g 13 mmol, 42 %. Measured spectra were in agreement with those in literature.[21] **^{1}H NMR** (500 MHz, DMSO) δ 8.90 (d, J = 2.2 Hz, 1H), 8.58 (dd, J = 4.7, 1.6 Hz, 1H), 8.18 (dt, J = 8.0, 2.0 Hz, 1H), 8.15 (dd, J = 7.9, 1.0 Hz, 1H), 7.82 (ddd, J = 8.4, 7.1, 1.6 Hz, 1H), 7.77 (d, J = 15.3 Hz, 1H), 7.69 (d, J = 7.9 Hz, 0H), 7.54 – 7.45 (m, 2H), 7.39 (d, J = 15.4 Hz, 1H), 7.26 – 7.19 (m, 4H), 7.19 – 7.11 (m, 1H), 4.54 (t, J = 7.5, 2H), 3.03 – 2.96 (t, J = 7.5 Hz, 2H). **^{13}C NMR** (126 MHz, DMSO) δ 161.62 (Cq), 152.38 (Cq), 150.70 (CH), 150.11 (CH), 147.53 (Cq), 138.67 (Cq), 136.93 (CH), 135.04 (CH), 134.98 (CH), 131.55 (Cq), 129.50 (CH), 128.97 (CH), 127.63 (CH), 127.11 (CH), 127.08 (CH), 126.89 (CH), 124.39

(CH), 122.18 (CH), 120.57 (Cq), 44.62 (CH_2), 34.91 (CH_2). **HR-MS** $[M+H]^+$: 354.16009 (calculated); 354.15983 (measured).

4.10.9.4 [Ru(tpy)(biq)(B0Cl)]Cl_2 ([1]Cl_2)

A solution of [Ru(tpy)(biq)Cl]Cl (102 mg, 0.17 mmol, 1 eq), **B0Cl** (131 mg, 0.35 mmol, 2 eq) and $AgPF_6$ (98.9 mg, 0.39 mol, 2 eq) in degassed acetone (50 mL) was stirred overnight at 70 °C under nitrogen atmosphere. The reaction mixture was filtered, and the filtrate was dried in vacuo. The resulting solids were dissolved in acetone (10 mL) and precipitated by the addition of saturated NEt_4Cl in EtOAc (1 mL). The precipitate was collected by filtration and purified over a MeOH-based Sephadex LH-20 size exclusion column. The first fraction was collected and dried in vacuo to afford the title compound as a purple solid. Yield: 138 mg, 0.13 mmol, 78 %. Rf = 0.25 in 70:30 DCM:MeOH. **^{1}H NMR** (850 MHz, DMSO) δ 9.32 (dt, J = 9.3, 2.8 Hz, 1H), 9.20 (dd, J = 8.8, 2.8 Hz, 1H), 9.09 (m, 2H; 12), 8.94 (t, J = 6.7 Hz, 1H), 8.80 (dd, J = 8.4, 4.5 Hz, 1H), 8.59 (dd, J = 8.8, 2.8 Hz, 1H), 8.53 (dd, J = 8.1, 4.2 Hz, 1H), 8.43 (td, J = 8.1, 2.5 Hz, 2H), 8.25 (t, J = 7.3 Hz, 1H), 8.20 (t, J = 7.4 Hz, 1H), 8.15 (dt, J = 7.8, 1.8 Hz, 2H), 8.03 (d, J = 5.5 Hz, 1H), 8.01 (t, J = 7.5 Hz, 1H), 7.96 (dt, J = 8.1, 2.0 Hz, 1H), 7.85 (tt, J = 7.7, 1.9 Hz, 1H), 7.79 (d, J = 2.1 Hz, 1H), 7.72 – 7.68 (m, 1H), 7.66 (d, J = 5.6 Hz, 1H), 7.61 (dd, J = 8.1, 2.3 Hz, 1H), 7.57 – 7.48 (m, 4H), 7.32 (dd, J = 8.7, 2.2 Hz, 2H), 7.29 (ddd, J = 8.5, 6.9, 1.6 Hz, 1H), 7.27 – 7.24 (m, 1H), 7.23 (dt, J = 7.1, 4.0 Hz, 3H), 7.16 (td, J = 6.1, 2.9 Hz, 3H), 6.57 (d, J = 9.0 Hz, 1H), 5.55 (d, J = 16.8 Hz, 1H), 5.49 (dd, J = 106.4, 16.6 Hz, 2H). **^{13}C NMR** (214 MHz, DMSO) δ 161.27 (Cq), 160.44 (Cq), 159.00 (Cq), 158.02 (Cq), 157.74 (Cq), 157.34 (Cq), 154.03(CH), 152.76 (CH), 151.23 (Cq), 150.68 (CH) 149.98 (Cq), 149.39 (Cq), 146.71 (Cq), 139.80 (CH), 139.19 (CH), 139.00 (CH), 138.63 (CH), 137.20 (CH), 136.09 (Cq), 135.03 (CH), 133.99 (CH), 133.26 (Cq), 131.95 (Cq), 131.37 (CH), 130.75 (CH), 130.19 (Cq), 130.03 (CH), 129.69 (CH), 128.65 (CH), 128.13 (Cq), 127.27 (CH), 127.07 (CH), 126.76 (CH), 126.16 (CH), 125.85 (CH), 125.00 (CH), 124.49 (CH), 124.26 (CH), 124.11 (CH), 122.87 (CH), 121.71 (CH), 121.37 (CH), 120.10 (Cq), 44.67 (CH_2). **HR-MS** $[M-2Cl]^{2+}$: 482.09897 (calculated); 482.09820 (measured). **Elem. Anal**. Calc. for $[C_{55}H_{39}Cl_3N_8ORu]$: C 63.80; H 3.80; N 10.82. Found: C 62.93; H 3.98; N 10.41.

4.10.9.5 [Ru(tpy)(biq)(B02)]Cl_2 ([2]Cl_2)

Compound [**2**]Cl_2 was synthesized according to the procedure described above for [**1**]Cl_2. Starting [Ru(tpy)(biq)Cl]Cl (0.18 mmol scale) but with B02 instead of B0Cl to afford the title compound as yellow needles. Yield: 89 mg, 0.09 mmol, 55 %.**^{1}H NMR** (600 MHz, DMSO) δ 9.16 (d, J = 8.9 Hz, 1H), 9.06 (d, J = 8.8 Hz, 1H), 8.89 (d, J = 8.8 Hz, 1H), 8.86 (d, J = 8.4 Hz, 1H), 8.70 (d, J = 8.2 Hz, 1H), 8.64 (d, J = 8.3 Hz, 1H), 8.46 (d, J = 8.8 Hz, 1H), 8.42 (d, J = 8.5 Hz, 1H), 8.38 – 8.30 (m, 2H), 8.22 (d, J = 8.1 Hz, 1H), 8.15 – 8.09 (m, 1H), 7.98 (s, 1H), 7.89 – 7.77 (m, 2H), 7.70 (t, J = 6.7 Hz, 2H), 7.66 (d, J = 8.1 Hz, 2H), 7.55 (t, J = 7.6 Hz, 1H), 7.52 – 7.41 (m, 3H), 7.33 – 7.25 (m, 6H), 7.23 (dd, J = 15.5,

3.0 Hz, 1H), 7.19 – 7.08 (m, 3H), 7.02 (dd, J = 15.5, 3.1 Hz, 1H), 6.72 (dd, J = 8.8, 3.1 Hz, 1H), 5.52 (d, J = 16.5 Hz, 1H), 5.40 (d, J = 16.3 Hz, 1H). **^{13}C NMR** (151 MHz, DMSO) δ 161.65 (Cq), 159.82 (Cq), 158.74 (Cq), 157.80 (Cq), 157.68 (Cq), 157.52 (Cq), 152.99 (CH), 151.91 (CH), 151.06 (Cq), 150.75 (CH), 150.53 (CH), 150.11 (Cq), 148.99 (Cq), 146.44 (Cq), 139.30 (CH), 138.50 (CH), 138.37 (CH), 138.21 (CH), 136.60 (CH), 135.98 (Cq), 134.61 (CH), 134.15 (CH), 133.38 (Cq), 133.25 (CH), 130.76 (CH), 130.59 (CH), 129.80 (Cq), 129.56 (CH), 128.85 (CH), 128.49 (CH), 128.14 (CH), 128.11 (CH), 128.01 (CH), 127.92 (CH), 126.93 (CH), 126.80 (CH), 126.67 (CH), 126.25 (CH), 125.99 (CH), 125.56 (CH), 125.51 (CH), 124.65 (CH), 123.93 (CH), 123.83 (CH), 123.57 (CH), 123.35 (CH), 122.54 (CH), 120.64 (CH), 120.26 (CH), 119.59 (Cq), 45.23 (CH_2).**HR-MS** $[M\text{-}2Cl]^{2+}$: 465.11862 (calculated); 465.11782 (measured). **Elem. Anal**. Calc. for $[C_{55}H_{40}Cl_2N_8ORu]$: C 66.00; H 4.03; N 11.19. Found: C 65.74; H 4.38; N 10.89.

4

4.10.9.6 [Ru(tpy)(biq)(B0Ref)]Cl_2 ([3]Cl_2)

Compound [**3**]Cl_2 was synthesized according to the procedure for [**1**]Cl_2. Starting [Ru(tpy)(biq)Cl]Cl (0.18 mmol scale) but with B0Ref instead of B0Cl to afford the title compound as yellow needles. Yield: 83 mg, 0.08 mmol, 55 %. **^{1}H NMR** (850 MHz, DMSO) δ 9.35 (d, J = 8.9 Hz, 1H), 9.22 (d, J = 8.8 Hz, 1H), 9.14 (d, J = 8.4 Hz, 1H), 9.10 (d, J = 8.8 Hz, 1H), 8.98 (d, J = 8.1 Hz, 1H), 8.88 (d, J = 8.1 Hz, 1H), 8.61 (d, J = 8.8 Hz, 1H), 8.47 (t, J = 8.9 Hz, 1H), 8.28 (d, J = 8.1 Hz, 1H), 8.24 – 8.20 (m, 1H), 8.18 (d, J = 5.6 Hz, 1H), 8.11 (dd, J = 14.4, 6.0 Hz, 2H), 8.04 (t, J = 7.7 Hz, 0H), 7.97 (d, J = 6.5 Hz, 1H), 7.81 (t, J = 6.8 Hz, 1H), 7.79 (s, 1H), 7.74 (t, J = 7.2 Hz, 1H), 7.69 (d, J = 5.6 Hz, 1H), 7.58 – 7.49 (m, 5H), 7.35 (ddd, J = 8.3, 6.5, 1.5 Hz, 1H), 7.33 – 7.28 (m, 2H), 7.25 (d, J = 8.9 Hz, 1H), 7.07 (d, J = 6.4 Hz, 2H), 7.05 – 7.02 (m, 4H), 6.92 (tt, J = 5.8, 2.6 Hz, 1H), 6.60 (d, J = 8.9 Hz, 1H), 4.43 (dt, J = 14.5, 7.3 Hz, 1H), 4.36 (dt, J = 14.4, 7.3 Hz, 1H), 2.84 (dq, J = 24.0, 6.8 Hz, 2H). **^{13}C NMR** (214 MHz, DMSO) δ 160.76 (Cq), 160.34 (Cq), 158.91 (Cq), 157.91 (Cq), 157.72 (Cq), 157.65 (Cq), 157.26 (Cq), 153.92 (CH), 152.76 (CH), 152.28 (CH), 151.31 (Cq), 150.38 (CH), 149.88 (Cq), 149.32 (Cq), 146.52 (Cq), 139.68, 139.11, 138.91, 138.51, 137.82 (Cq), 137.14, 135.20, 134.49, 133.45 (Cq), 133.02 (CH), 131.24 (CH), 130.78 (CH), 130.10 (Cq), 129.93 (CH), 129.57 (CH), 128.89 (CH), 128.81 (CH), 128.79 (CH), 128.64 (CH), 128.52 (CH), 128.35 (CH), 128.13 (CH), 128.02 (Cq), 126.82 (CH), 126.36 (CH), 126.34 (CH), 126.06 (CH), 125.98 (CH), 125.69 (CH), 124.88 (CH), 124.42 (CH), 124.14 (CH), 122.76 (CH), 121.62 (CH), 121.27 (CH), 119.97 (Cq), 43.94 (CH_2), 34.03 (CH_2). **HR-MS** $[M\text{-}2Cl]^{2+}$: 472.12646 (calculated); 472.12579 (measured). **Elem. Anal**. Calc. for $[C_{56}H_{42}Cl_2N_8ORu]$: C 66.27; H 4.17; N 11.04. Found: C 66.13; H 4.49; N 10.78.

4.10.9.7 [Ru(tpy)(biq)(Py)]Cl_2 ([4]Cl_2)

A solution of [Ru(tpy)(biq)(CL)]Cl (170 mg, 0.26 mmol), $AgPF_6$ (197 mg, 0.62 mmol) and pyridine (0.5 mL) in deoxygenated aceton (15 mL) was refluxed overnight under

nitrogen atmosphere. The solution was filtered, and the filtrate was concentrated and dissolved in a minimal amount of acetone (5 mL) to which EtOAc (5 mL) was added. Subsequently a saturated NEt_4Cl in EtOAc solution (1 mL) and EtOAc (10 mL) was added and the formed precipitate was filtered, washed with EtOAc (40 mL), diethylether (2 x 40 mL) and dried in vacuo to afford the title compound as a dark red/pink powder. Yield: 131 mg, 0.18 mmol, 69 %.**^{1}H NMR** (600 MHz, MeOD) δ 9.14 (d, J = 8.8 Hz, 1H), 9.04 (d, J = 8.8 Hz, 1H), 8.87 (d, J = 8.8 Hz, 1H), 8.76 (d, J = 8.1 Hz, 2H), 8.59 – 8.55 (m, 2H), 8.44 (d, J = 8.7 Hz, 1H), 8.36 (d, J = 8.1 Hz, 1H), 8.33 (t, J = 8.1 Hz, 1H), 8.08 – 8.02 (m, 4H), 7.86 (d, J = 1.5 Hz, 0H), 7.74 (ddd, J = 8.0, 4.5, 3.3 Hz, 1H), 7.70 (dtd, J = 6.2, 3.8, 3.2, 1.2 Hz, 3H), 7.48 (t, J = 7.5 Hz, 1H), 7.45 (dd, J = 7.5, 5.7 Hz, 2H), 7.32 – 7.25 (m, 3H), 7.06 (t, J = 7.1 Hz, 2H), 6.75 (d, J = 8.9 Hz, 1H). **^{13}C NMR** (151 MHz, MeOD) δ 159.61 (Cq), 158.53 (Cq), 157.58 (Cq), 157.55 (CH), 152.27 (CH), 150.51 (Cq), 149.99 (Cq), 148.95 (CH), 138.95 (CH), 138.07 (CH), 137.86 (CH), 137.77 (CH), 136.17 (CH), 130.50 (CH), 130.33 (CH), 129.60 (Cq), 129.25 (CH), 128.61 (CH), 128.20 (CH), 127.86 (CH), 127.82 (Cq), 127.69 (CH), 125.30 (CH), 125.27 (CH), 124.01 (CH), 123.31 (CH), 122.44 (CH), 120.33 (CH), 120.04 (CH). **HR-MS** $[M\text{-}Cl\text{-}Py]^+$: 626.06855 (calculated); 626.06702 (measured). **Elem. Anal**. Calc. for $[C_{38}H_{28}Cl_2N_6Ru]$: C 61.62; H 3.81; N 11.35. Found: C 61.44; H 4.21; N 11.02.

4.10.9.8 [Ru(tpy)(dppz)(B0Cl)]Cl_2 ([5]Cl_2)

A solution of [Ru(tpy)(dppz)Cl]Cl (67.5 mg, 0.1 mmol, 1 eq), B0Cl (80.2 mg, 0.21 mmol, 2 eq) and $AgPF_6$ (55.7 mg, 0.22 mmol, 2 eq) in degassed acetone (25 ml) was stirred overnight at 70 °C under nitrogen atmosphere. The reaction mixture was left to cool to RT and filtered and the residue was washed with acetone (10 mL). The filtrate was concentrated in vacuo and purified over silica column with a length of 15 cm and diameter of 3 cm (DCM:MeOH 100:0 → 50:50). The orange fraction was collected (Rf = 0.21 in DCM: MeOH 70:30), dried in vacuo, dissolved in acetone (15 mL), and precipitated by the addition of a saturated solution of NEt_4Cl in EtOAc (~ 1 mL) and EtOAc (15 mL). The precipitate was filtered and washed with EtOAc (40 mL), diethyl ether (2 x 40 mL) and dried in vacuo to afford the title compound as a red solid. Yield: 85 mg, 0.08 mmol, 83 %. Rf = 0.21 in DCM:MeOH 70:30. **^{1}H NMR** (850 MHz, DMSO) δ 9.89 (dd, J = 8.1, 1.3 Hz, 1H), 9.43 (dd, J = 7.9, 1.3 Hz, 1H), 9.24 – 9.21 (m, 1H), 8.96 (d, J = 8.2 Hz, 2H), 8.81 (d, J = 8.1 Hz, 2H), 8.59 (dd, J = 8.5, 1.5 Hz, 1H), 8.50 – 8.45 (m, 2H), 8.43 (t, J = 8.2 Hz, 1H), 8.39 (d, J = 8.1 Hz, 1H), 8.32 (d, J = 1.9 Hz, 1H), 8.22 (ddd, J = 8.4, 6.7, 1.5 Hz, 1H), 8.20 – 8.16 (m, 2H), 8.12 – 8.08 (m, 2H), 7.93 – 7.90 (m, 2H), 7.89 – 7.85 (m, 1H), 7.84 – 7.81 (m, 1H), 7.73 (d, J = 15.3 Hz, 1H), 7.71 (dd, J = 8.0, 5.4 Hz, 1H), 7.69 (d, J = 8.2 Hz, 1H), 7.61 (d, J = 5.6 Hz, 1H), 7.57 (t, J = 7.6 Hz, 1H), 7.42 (t, J = 6.5 Hz, 1H), 7.39 (dd, J = 8.1, 5.7 Hz, 1H), 7.36 (d, J = 15.4 Hz, 1H), 7.34 (d, J = 8.3 Hz, 2H), 7.23 (d, J = 8.2 Hz, 2H), 5.55 (s, 2H). ^{13}C NMR (214 MHz, DMSO) δ 161.35 (Cq), 157.69 (Cq), 157.22 (Cq), 154.13 (CH), 153.59 (CH), 153.07 (CH), 152.76 (CH), 151.91 (CH),

151.26 (Cq), 150.63 (Cq), 149.66 (Cq), 146.82 (Cq), 142.09 (Cq), 141.96 (Cq), 140.43 (Cq), 140.03 (Cq), 138.77 (CH), 136.64 (CH), 136.06 (Cq), 135.05 (CH), 134.98 (CH), 134.92 (CH), 133.78 (Cq), 132.97 (CH), 132.87 (CH), 132.66 (CH), 132.59 (CH), 131.96 (Cq), 130.33 (Cq), 129.53 (CH), 129.49 (CH), 129.48 (Cq), 128.75 (CH), 128.61 (CH), 128.51 (CH), 127.86 (CH), 127.26 (CH), 127.16 (CH), 126.89 (CH), 126.75 (CH), 126.42 (CH), 125.09 (CH), 124.38 (CH), 123.82 (CH), 120.13 (Cq), 44.84 (CH_2).**HR-MS** $[M\text{-}2Cl]^{2+}$: 495.09421 (calculated); 495.09322 (measured). **Elem. Anal**. Calc. for $[C_{55}H_{37}Cl_3N_{10}ORu] + H_2O$: C 61.20; H 3.64; N 12.98. Found: C 61.39; H 3.54; N 12.73.

4.10.9.9 [Ru(tpy)(dppn)(B0Cl)]Cl_2 ([6]Cl_2)

A solution of [Ru(tpy)(dppn)Cl]Cl (124 mg, 0.17 mmol, 1 eq), B0Cl (344 mg, 0.92 mmol, 5.5 eq) and AgPF6 (229 mg, 0.91 mmol, 5.5 eq) in degassed acetone (50 ml) was stirred for 3 days at 70 °C under nitrogen atmosphere. The reaction mixture was left to cool to RT and filtered. The filtrate was concentrated in vacuo and purified over silica (DCM:MeOH 99.7:0.3 → 90:10). The brown-orange fraction was collected (Rf = 0.21 DCM:MeOH 70:30) and dried in vacuo. The solid was dissolved in acetone (15 mL) and was precipitated by the addition of a saturated solution of $NCl(Et)_4$ in EtOAc (~ 1 mL) and EtOAc (15 mL). The precipitate was filtered and washed with EtOAc (200 mL) and diethyl ether (2 x 100 mL) and dried overnight under vacuo to afford the title compound as a red solid. Yield: 128 mg, 0.12 mmol, 69 %. Rf = 0.21 DCM:MeOH 70:30 **^{1}H NMR** (850 MHz, DMSO) δ 9.87 (d, J = 8.1 Hz, 1H), 9.41 (d, J = 7.8 Hz, 1H), 9.31 (s, 1H), 9.22 (s, 1H), 9.19 (d, J = 5.1 Hz, 1H), 8.99 (d, J = 8.3 Hz, 2H), 8.84 (d, J = 8.1 Hz, 2H), 8.48 (dd, J = 8.4, 5.5 Hz, 2H), 8.44 (d, J = 7.7 Hz, 2H), 8.41 (d, J = 8.1 Hz, 1H), 8.34 (s, 1H), 8.18 (d, J = 7.9 Hz, 1H), 8.12 (t, J = 7.7 Hz, 2H), 7.96 (s, 2H), 7.87 (t, J = 7.8 Hz, 1H), 7.82 – 7.77 (m, 3H), 7.74 (d, J = 15.3 Hz, 1H), 7.72 – 7.68 (m, 2H), 7.62 (d, J = 5.6 Hz, 1H), 7.57 (t, J = 7.5 Hz, 1H), 7.45 (t, J = 6.6 Hz, 2H), 7.42 – 7.37 (m, 2H), 7.35 (d, J = 8.1 Hz, 2H), 7.24 (d, J = 8.1 Hz, 2H), 5.57 (s, 2H). **^{13}C NMR** (214 MHz, DMSO) δ 161.23 (Cq), 157.58 (Cq), 157.10 (Cq), 153.99 (CH), 153.52 (CH), 152.95 (CH), 152.69 (CH), 151.78 (CH), 151.23 (Cq), 151.15 (Cq), 150.21 (Cq), 146.71 (Cq), 141.33 (Cq), 140.94 (Cq), 138.65 (CH), 137.98 (Cq), 137.88 (Cq), 136.51 (CH), 135.97 (Cq), 134.93 (CH), 134.84 (CH), 134.82 (CH), 134.57 (Cq), 134.52 (Cq), 133.68 (Cq), 132.84 (CH), 132.73 (CH), 131.84 (Cq), 130.63 (Cq), 129.78 (Cq), 128.63 (CH), 128.56 (CH), 128.49 (CH), 128.41 (CH), 127.98 (CH), 127.94 (CH), 127.88 (CH), 127.13 (CH), 127.04 (CH), 126.95 (CH), 126.63 (CH), 126.30 (CH), 125.00 (CH), 124.28 (CH), 123.71 (CH), 120.03 (Cq), 44.72 (CH_2).**HR-MS** $[M\text{-}2Cl]^{2+}$: 520.10209 (calculated); 520.10147 (measured). **Elem. Anal**. Calc. for $[C_{59}H_{39}Cl_3N_{10}ORu]$: C 63.76; H 3.54; N 12.60. Found: C 63.28; H 3.78; N 12.38.

4.11 Literature

(1) Lameijer, L. N.; Ernst, D.; Hopkins, S. L.; Meijer, M. S.; Askes, S. H. C.; Le Dévédec, S. E.; Bonnet, S. A Red-Light-Activated Ruthenium-Caged NAMPT Inhibitor Remains Phototoxic in Hypoxic Cancer Cells. *Angew. Chem. Int. Ed.* **2017**, *56* (38), 11549–11553.

(2) van Rixel, V. H. S.; Ramu, V.; Auyeung, A. B.; Beztsinna, N.; Leger, D. Y.; Lameijer, L. N.; Hilt, S. T.; Le Dévédec, S. E.; Yildiz, T.; Betancourt, T.; Gildner, M. B.; Hudnall, T. W.; Sol, V.; Liagre, B.; Kornienko, A.; Bonnet, S. Photo-Uncaging of a Microtubule-Targeted Rigidin Analogue in Hypoxic Cancer Cells and in a Xenograft Mouse Model. *J. Am. Chem. Soc.* **2019**, *141* (46), 18444–18454.

(3) Respondek, T.; Garner, R. N.; Herroon, M. K.; Podgorski, I.; Turro, C.; Kodanko, J. J. Light Activation of a Cysteine Protease Inhibitor: Caging of a Peptidomimetic Nitrile with RuII(Bpy)2. *J. Am. Chem. Soc.* **2011**, *133* (43), 17164–17167.

(4) Ramalho, S. D.; Sharma, R.; White, J. K.; Aggarwal, N.; Chalasani, A.; Sameni, M.; Moin, K.; Vieira, P. C.; Turro, C.; Kodanko, J. J.; Sloane, B. F. Imaging Sites of Inhibition of Proteolysis in Pathomimetic Human Breast Cancer Cultures by Light-Activated Ruthenium Compound. *PLOS ONE* **2015**, *10* (11), e0142527.

(5) van de Griend, C.; van de Vijver, J. J.; Siegler, M. A.; Dame, R. T.; Bonnet, S. Ruthenium-Locked Helical Chirality: A Barrier of Inversion and Formation of an Asymmetric Macrocycle. *Inorg. Chem.* **2022**, *61* (40), 16045–16054.

(6) Cuello-Garibo, J.-A.; Meijer, M. S.; Bonnet, S. To Cage or to Be Caged? The Cytotoxic Species in Ruthenium-Based Photoactivated Chemotherapy Is Not Always the Metal. *Chem. Commun.* **2017**, *53* (50), 6768–6771.

(7) Lim, M. H.; Song, H.; Olmon, E. D.; Dervan, E. E.; Barton, J. K. Sensitivity of Ru(Bpy)2dppz2+ Luminescence to DNA Defects. *Inorg. Chem.* **2009**, *48* (12), 5392–5397.

(8) Havrylyuk, D.; Stevens, K.; Parkin, S.; Glazer, E. C. Toward Optimal Ru(II) Photocages: Balancing Photochemistry, Stability, and Biocompatibility Through Fine Tuning of Steric, Electronic, and Physiochemical Features. *Inorg. Chem.* **2020**, *59* (2), 1006–1013.

(9) Lifshits, L. M.; III, J. A. R.; Ramasamy, E.; Thummel, R. P.; Cameron, C. G.; McFarland, S. A. Ruthenium Photosensitizers for NIR PDT Require Lowest-Lying Triplet Intraligand (3IL) Excited States. *J. Photochem. Photobiol.* **2021**, *8*, 100067.

(10) Zamora, A.; Denning, C. A.; Heidary, D. K.; Wachter, E.; Nease, L. A.; Ruiz, J.; Glazer, E. C. Ruthenium-Containing P450 Inhibitors for Dual Enzyme Inhibition and DNA Damage. *Dalton Trans* **2017**, *46* (7), 2165–2173.

(11) Rosenberg, B.; Van Camp, L.; Krigas, T. Inhibition of Cell Division in Escherichia Coli by Electrolysis Products from a Platinum Electrode. *Nature* **1965**, *205* (4972), 698–699.

(12) Sherman, S. E.; Lippard, S. J. Structural Aspects of Platinum Anticancer Drug Interactions with DNA. *Chem. Rev.* **1987**, *87* (5), 1153–1181.

(13) Jung, Y.; Lippard, S. J. Direct Cellular Responses to Platinum-Induced DNA Damage. *Chem. Rev.* **2007**, *107* (5), 1387–1407.

(14) Loehrer, P. J.; Einhorn, L. H. Cisplatin. *Ann. Intern. Med.* **1984**, *100* (5), 704–713.

(15) Cohen, S. M.; Lippard, S. J. Cisplatin: From DNA Damage to Cancer Chemotherapy. In *Progress in Nucleic Acid Research and Molecular Biology*; Academic Press, 2001; Vol. 67, pp 93–130.

(16) Huang, D.; Savage, S. R.; Calinawan, A. P.; Lin, C.; Zhang, B.; Wang, P.; Starr, T. K.; Birrer, M. J.; Paulovich, A. G. A Highly Annotated Database of Genes Associated with Platinum Resistance in Cancer. *Oncogene* **2021**, *40* (46), 6395–6405.

(17) Friedberg, E. C. DNA Damage and Repair. *Nature* **2003**, *421* (6921), 436–440.

(18) Kartalou, M.; Essigmann, J. M. Mechanisms of Resistance to Cisplatin. *Mutat. Res. Mol. Mech. Mutagen.* **2001**, *478* (1), 23–43.

(19) Schürmann, L.; Schumacher, L.; Roquette, K.; Brozovic, A.; Fritz, G. Inhibition of the DSB Repair Protein RAD51 Potentiates the Cytotoxic Efficacy of Doxorubicin via Promoting Apoptosis-Related Death Pathways. *Cancer Lett.* **2021**, *520*, 361–373.

(20) Alagpulinsa, D. A.; Ayyadevara, S.; Shmookler Reis, R. J. A Small-Molecule Inhibitor of RAD51 Reduces Homologous Recombination and Sensitizes Multiple Myeloma Cells to Doxorubicin. *Front. Oncol.* **2014**, *4*.

(21) Ward, A.; Dong, L.; Harris, J. M.; Khanna, K. K.; Al-Ejeh, F.; Fairlie, D. P.; Wiegmans, A. P.; Liu, L. Quinazolinone Derivatives as Inhibitors of Homologous Recombinase RAD51. *Bioorg. Med. Chem. Lett.* **2017**, *27* (14), 3096–3100.

(22) Jager, M. J.; Shields, C. L.; Cebulla, C. M.; Abdel-Rahman, M. H.; Grossniklaus, H. E.; Stern, M.-H.; Carvajal, R. D.; Belfort, R. N.; Jia, R.; Shields, J. A.; Damato, B. E. Uveal Melanoma. *Nat. Rev. Dis.*

Primer **2020**, *6* (1), 24.
(23) Yang, J.; Manson, D. K.; Marr, B. P.; Carvajal, R. D. Treatment of Uveal Melanoma: Where Are We Now? *Ther. Adv. Med. Oncol.* **2018**, *10*, 1758834018757175.
(24) Molphy, Z.; Prisecaru, A.; Slator, C.; Barron, N.; McCann, M.; Colleran, J.; Chandran, D.; Gathergood, N.; Kellett, A. Copper Phenanthrene Oxidative Chemical Nucleases. *Inorg. Chem.* **2014**, *53* (10), 5392–5404.
(25) Ovchinnikova, I. G.; Kim, G. A.; Matochkina, E. G.; Kodess, M. I.; Barykin, N. V.; El´tsov, O. S.; Nosova, E. V.; Rusinov, G. L.; Charushin, V. N. Synthesis, Photochemical and Luminescent Properties of (E)-2-(2-Hydroxyarylethylene)-3-Phenylquinazolin-4(3H)-Ones. *Russ. Chem. Bull.* **2014**, *63* (11), 2467–2477.
(26) Knoll, J. D.; Albani, B. A.; Turro, C. New Ru(II) Complexes for Dual Photoreactivity: Ligand Exchange and 1O2 Generation. *Acc. Chem. Res.* **2015**, *48* (8), 2280–2287.
(27) Knoll, J. D.; Albani, B. A.; Durr, C. B.; Turro, C. Unusually Efficient Pyridine Photodissociation from Ru(II) Complexes with Sterically Bulky Bidentate Ancillary Ligands. *J. Phys. Chem. A* **2014**, *118* (45), 10603–10610.
(28) Lameijer, L. N.; van de Griend, C.; Hopkins, S. L.; Volbeda, A.-G.; Askes, S. H. C.; Siegler, M. A.; Bonnet, S. Photochemical Resolution of a Thermally Inert Cyclometalated Ru(Phbpy)(N–N)(Sulfoxide)+ Complex. *J. Am. Chem. Soc.* **2019**, *141* (1), 352–362.
(29) Lifshits, L. M.; Roque III, J. A.; Konda, P.; Monro, S.; Cole, H. D.; von Dohlen, D.; Kim, S.; Deep, G.; Thummel, R. P.; Cameron, C. G.; Gujar, S.; McFarland, S. A. Near-Infrared Absorbing Ru(Ii) Complexes Act as Immunoprotective Photodynamic Therapy (PDT) Agents against Aggressive Melanoma. *Chem Sci* **2020**, *11* (43), 11740–11762.
(30) Bindra Ranjit S.; Schaffer Paul J.; Meng Alice; Woo Jennifer; Måseide Kårstein; Roth Matt E.; Lizardi Paul; Hedley David W.; Bristow Robert G.; Glazer Peter M. Down-Regulation of Rad51 and Decreased Homologous Recombination in Hypoxic Cancer Cells. *Mol. Cell. Biol.* **2004**, *24* (19), 8504–8518.
(31) Cosse, J.-P.; Michiels, C. Tumour Hypoxia Affects the Responsiveness of Cancer Cells to Chemotherapy and Promotes Cancer Progression. *Former. Curr. Med. Chem. - Anti-Cancer Agents* **2008**, *8* (7), 790–797.
(32) Zeng, L.; Chen, Y.; Huang, H.; Wang, J.; Zhao, D.; Ji, L.; Chao, H. Cyclometalated Ruthenium(II) Anthraquinone Complexes Exhibit Strong Anticancer Activity in Hypoxic Tumor Cells. *Chem. – Eur. J.* **2015**, *21* (43), 15308–15319.
(33) Cole, H. D.; Roque, J. A. I.; Shi, G.; Lifshits, L. M.; Ramasamy, E.; Barrett, P. C.; Hodges, R. O.; Cameron, C. G.; McFarland, S. A. Anticancer Agent with Inexplicable Potency in Extreme Hypoxia: Characterizing a Light-Triggered Ruthenium Ubertoxin. *J. Am. Chem. Soc.* **2022**, *144* (22), 9543–9547.
(34) Devarajan, N.; Manjunathan, R.; Ganesan, S. K. Tumor Hypoxia: The Major Culprit behind Cisplatin Resistance in Cancer Patients. *Crit. Rev. Oncol. Hematol.* **2021**, *162*, 103327.
(35) Cohen, S. M.; Lippard, S. J. Cisplatin: From DNA Damage to Cancer Chemotherapy. In *Progress in Nucleic Acid Research and Molecular Biology*; Academic Press, 2001; Vol. 67, pp 93–130.
(36) Pages, B. J.; Ang, D. L.; Wright, E. P.; Aldrich-Wright, J. R. Metal Complex Interactions with DNA. *Dalton Trans* **2015**, *44* (8), 3505–3526.
(37) Chen, T.; Tongpeng, S.; Lu, Z.; Topatana, W.; Juengpanich, S.; Li, S.; Hu, J.; Cao, J.; Lee, C.; Tian, Y.; Chen, M.; Cai, X. DNA Damage Response Inhibition-Based Combination Therapies in Cancer Treatment: Recent Advances and Future Directions. *Aging Cancer* **2022**, *3* (1), 44–67.
(38) Deans, A. J.; West, S. C. DNA Interstrand Crosslink Repair and Cancer. *Nat. Rev. Cancer* **2011**, *11* (7), 467–480.
(39) Riddell, I. A.; Lippard, S. J. Metallo-Drugs: Development and Action of Anticancer Agents; Sigel, A., Sigel, H., Freisinger, E., Sigel, R. K. O., Eds.; De Gruyter, 2018; pp 1–42.
(40) Ceccaldi, R.; Sarangi, P.; D'Andrea, A. D. The Fanconi Anaemia Pathway: New Players and New Functions. *Nat. Rev. Mol. Cell Biol.* **2016**, *17* (6), 337–349.
(41) Jalal, S.; Earley, J. N.; Turchi, J. J. DNA Repair: From Genome Maintenance to Biomarker and Therapeutic Target. *Clin. Cancer Res.* **2011**, *17* (22), 6973–6984.
(42) Moldovan, G.-L.; D'Andrea, A. D. How the Fanconi Anemia Pathway Guards the Genome. *Annu. Rev. Genet.* **2009**, *43* (1), 223–249.
(43) Kiss, R. C.; Xia, F.; Acklin, S. Targeting DNA Damage Response and Repair to Enhance Therapeutic Index in Cisplatin-Based Cancer Treatment. *Int. J. Mol. Sci.* **2021**, *22* (15).
(44) Yang, L.-Y.; Li, L.; Jiang, H.; Shen, Y.; Plunkett, W. Expression of ERCC1 Antisense RNA Abrogates Gemcitabine-Mediated Cytotoxic Synergism with Cisplatin in Human Colon Tumor Cells Defec-

tive in Mismatch Repair but Proficient in Nucleotide Excision Repair1. *Clin. Cancer Res.* **2000**, *6* (3), 773–781.

(45) Duan, M.; Ulibarri, J.; Liu, K. J.; Mao, P. Role of Nucleotide Excision Repair in Cisplatin Resistance. *Int. J. Mol. Sci.* **2020**, *21* (23), 9248.

(46) Lee, J. O.; Kang, M. J.; Byun, W. S.; Kim, S. A.; Seo, I. H.; Han, J. Ah.; Moon, J. W.; Kim, J. H.; Kim, S. J.; Lee, E. J.; In Park, S.; Park, S. H.; Kim, H. S. Metformin Overcomes Resistance to Cisplatin in Triple-Negative Breast Cancer (TNBC) Cells by Targeting RAD51. *Breast Cancer Res.* **2019**, *21* (1), 115.

(47) He, W.-L.; Li, Y.-H.; Hou, W.-J.; Ke, Z.-F.; Chen, X.-L.; Lu, L.-Y.; Cai, S.-R.; Song, W.; Zhang, C.-H.; He, Y.-L. RAD51 Potentiates Synergistic Effects of Chemotherapy with PCI-24781 and Cis-Diamminedichloroplatinum on Gastric Cancer. *World J. Gastroenterol. WJG* **2014**, *20* (29), 10094.

(48) Abuzeid, W. M.; Jiang, X.; Shi, G.; Wang, H.; Paulson, D.; Araki, K.; Jungreis, D.; Carney, J.; O'Malley, B. W., Jr.; Li, D. Molecular Disruption of RAD50 Sensitizes Human Tumor Cells to Cisplatin-Based Chemotherapy. *J. Clin. Invest.* **2009**, *119* (7), 1974–1985.

(49) Stronach, E. A.; Chen, M.; Maginn, E. N.; Agarwal, R.; Mills, G. B.; Wasan, H.; Gabra, H. DNA-PK Mediates AKT Activation and Apoptosis Inhibition in Clinically Acquired Platinum Resistance. *Neoplasia* **2011**, *13* (11), 1069-IN35.

(50) Jacquemont, C.; Simon, J. A.; D'Andrea, A. D.; Taniguchi, T. Non-Specific Chemical Inhibition of the Fanconi Anemia Pathway Sensitizes Cancer Cells to Cisplatin. *Mol. Cancer* **2012**, *11* (1), 26.

(51) Chirnomas, D.; Taniguchi, T.; de la Vega, M.; Vaidya, A. P.; Vasserman, M.; Hartman, A.-R.; Kennedy, R.; Foster, R.; Mahoney, J.; Seiden, M. V.; D'Andrea, A. D. Chemosensitization to Cisplatin by Inhibitors of the Fanconi Anemia/BRCA Pathway. *Mol. Cancer Ther.* **2006**, *5* (4), 952–961.

(52) Taymaz-Nikerel, H.; Karabekmez, M. E.; Eraslan, S.; Kırdar, B. Doxorubicin Induces an Extensive Transcriptional and Metabolic Rewiring in Yeast Cells. *Sci. Rep.* **2018**, *8* (1), 13672.

(53) Roychoudhury, S.; Kumar, A.; Bhatkar, D.; Sharma, N. K. Molecular Avenues in Targeted Doxorubicin Cancer Therapy. *Future Oncol.* **2020**, *16* (11), 687–700.

(54) Ciszewski, W. M.; Tavecchio, M.; Dastych, J.; Curtin, N. J. DNA-PK Inhibition by NU7441 Sensitizes Breast Cancer Cells to Ionizing Radiation and Doxorubicin. *Breast Cancer Res. Treat.* **2014**, *143* (1), 47–55.

(55) Kumar, A.; Bhatkar, D.; Jahagirdar, D.; Sharma, N. K. Non-Homologous End Joining Inhibitor SCR-7 to Exacerbate Low-Dose Doxorubicin Cytotoxicity in HeLa Cells. *J. Cancer Prev.* **2017**, *22* (1), 47–54.

(56) Faraoni, I.; Graziani, G. Role of BRCA Mutations in Cancer Treatment with Poly(ADP-Ribose) Polymerase (PARP) Inhibitors. *Cancers* **2018**, *10* (12).

(57) Mårtensson, A. K. F.; Lincoln, P. Binding of Ru(Terpyridine)(Pyridine)Dipyridophenazine to DNA Studied with Polarized Spectroscopy and Calorimetry. *Dalton Trans.* **2015**, *44* (8), 3604–3613.

(58) Zhou, X.-Q.; Busemann, A.; Meijer, M. S.; Siegler, M. A.; Bonnet, S. The Two Isomers of a Cyclometallated Palladium Sensitizer Show Different Photodynamic Properties in Cancer Cells. *Chem. Commun.* **2019**, *55* (32), 4695–4698.

(59) Calvert, J.; Pitts, J. Chemical Actinometer for the Determination of Ultraviolet Light Intensities. *Photo Chem. Wiley Sons N. Y.* **1967**, 780.

(60) Bahreman, A.; Limburg, B.; Siegler, M. A.; Bouwman, E.; Bonnet, S. Spontaneous Formation in the Dark, and Visible Light-Induced Cleavage, of a Ru–S Bond in Water: A Thermodynamic and Kinetic Study. *Inorg. Chem.* **2013**, *52* (16), 9456–9469.